

A COMPARATIVE STUDY OF GRAPHITE GROWTH IN CAST IRON AND IN ANALOGOUS SYSTEMS

D.M. Stefanescu

Ohio State University, Columbus, OH, USA
University of Alabama, Tuscaloosa, AL, USA

G. Alonso and P. Larrañaga

IK4-Azterlan, Durango, Biscay, Spain

E. De la Fuente

Veigalan Estudio 2010 S.L.U, Durango, Biscay, Spain

R. Suarez

IK4-Azterlan, Durango, Biscay, Spain
Veigalan Estudio 2010 S.L.U, Durango, Biscay, Spain

Copyright © 2018 American Foundry Society
<https://doi.org/10.1007/s40962-017-0204-1>

Abstract

Crystallization of graphite during the solidification and cooling of cast iron to room temperature has been the object of relentless, yet often inconclusive research. The importance of the subject cannot be underestimated, as graphite morphology is a major player in establishing the mechanical and physical properties of cast iron. Graphite crystallization is a complex phenomenon controlled by melt composition, local melt supersaturation, melt temperature and temperature gradient (cooling rate). All these are wide-ranging variables in the casting process. The results of a major effort to understand the complexity of graphite crystallization in cast iron is presented in this comparative study of crystal growth in materials with crystal morphologies similar to that of graphite. The analysis includes that of analogous materials such as eutectic aluminum–

silicon and nickel carbon alloys, growth of other hexagonal or tetragonal crystals such as ice crystals and Al_3Ti in aluminum–titanium alloys, growth of graphite through other processing routes such as chemical vapor deposition (a gas-to-solid transformation), and heat treatment of carbon steel (a solid-to-solid transformation), and the previous information on the crystallization of carbon in cast irons. An exhaustive analysis of the most widely accepted models for graphite growth is also presented.

Keywords: cast iron, graphite morphology, foliated dendrites, lamellar graphite, compacted graphite, chunky graphite, spheroidal graphite, graphite growth

Introduction

There are several allotropes of carbon based on a hexagonal lattice, as summarized in Figure 1.¹ Graphite is one of the two naturally occurring forms of crystalline carbon. The other natural allotrope is diamond. Above 900 °C, the diamond structure is transformed into graphite. While diamond has a face-centered cubic Bravais lattice, graphite has structured graphene layers in which the carbon atoms are arranged in a honeycomb lattice with separation of

0.142 nm and distance between planes of 0.335 nm. The strong sigma bonds (a covalent bond resulting from the formation of a molecular orbital by the end-to-end overlap of atomic orbitals) in layers and weak Pi bonds (a covalent bond resulting from the formation of a molecular orbital by side-to-side overlap of atomic orbitals along a plane perpendicular to a line connecting the nuclei of the atoms) between layers produce the faceted morphology and high anisotropic behavior of graphite.

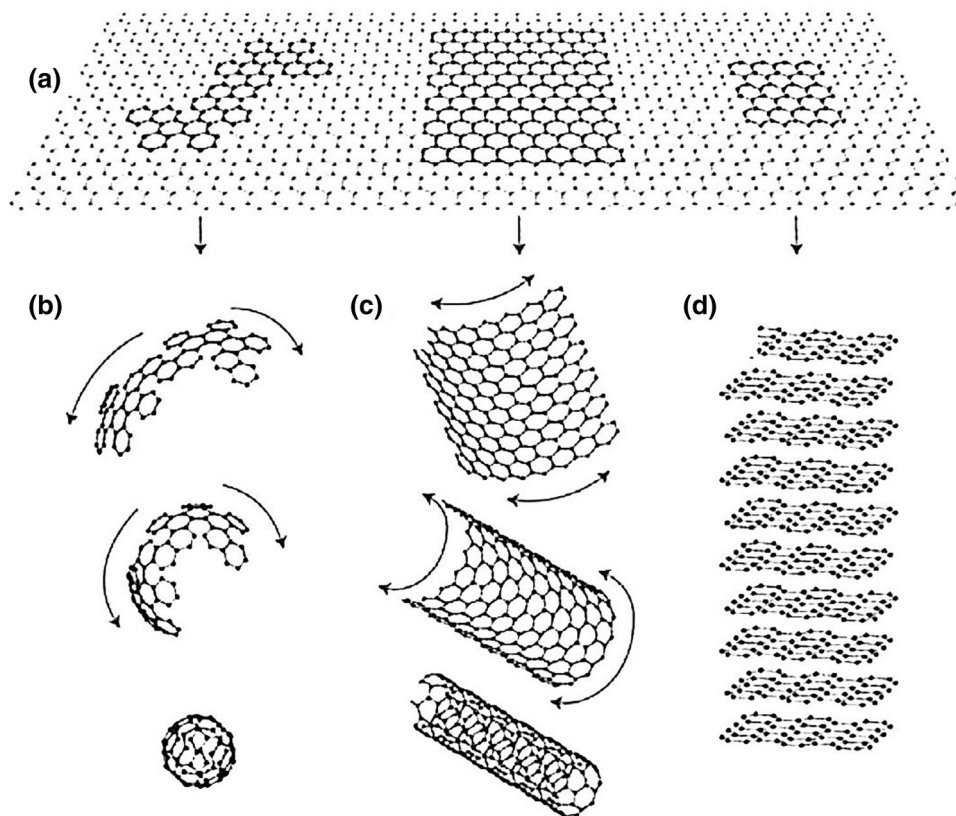


Figure 1. Allotropes of carbon: (a) 2-D graphene (b) 0-D fullerene, (c) 1-D carbon nanotube, (d) 3-D graphite.¹

As suggested by the Bravais's rule and the Gibbs–Wulff theorem, typically graphite grows faster along the tightly bond *a*-axis directions [1010], rather than the loosely bond *c*-axis direction [0001]. This explains the graphite flakes found in natural graphite and the graphite lamellae in gray cast iron. However, in nickel–carbon, cobalt–carbon and iron–carbon alloys, such as steel and cast iron, spheroidal graphite can be produced, where the graphite aggregate appears to extend in the *c*-direction rather than the *a*-direction, producing spheroidal (nodular) graphite.

The quest for complete understanding of the mechanisms involved in the genesis of the graphite morphology in cast iron is still the subject of much research. Room temperature graphite morphology in cast Fe–C alloys is the result of crystallization from the liquid controlled by attachment kinetics, followed by solid-state carbon diffusion growth and crystallization. The chemical complexity of the iron melts, and the transitory nature of nucleation, local segregation and cooling rate, are the reasons for the large variety of graphite morphologies found in industrial cast irons. They include what are considered to be the “standard” shapes: lamellar/flake (LG), compacted/vermicular (CG), spheroidal/nodular (SG), and temper graphite (in malleable iron). In addition, some “degenerated” morphology, such as spiky, exploded, or chunky graphite, can result from incorrect melt treatment or unfavorable cooling conditions. Some typical examples of graphite shapes, obtained

through deep etching of metallographic samples and graphite extraction after complete dissolution of the iron matrix, illustrating the complex morphology whose genesis must be explained in this work, are presented in Figure 2.^{2–5}

Metallographic specimens of cast and cooled to room temperature Mg- or Ce-treated melts frequently exhibit a multilayer structure, associated with up to three stages in their formation. Two-stage (duplex) spheroids have also been observed.⁶

The graphite aggregates in Figure 3 display three-stage microstructures.⁷ The room temperature graphite spheroid is the product of three processes: (i) nucleation and growth in the liquid; (ii) growth during the eutectic transformation via carbon diffusion through the austenite shell; (iii) growth during cooling to room temperature as the solubility of carbon in austenite decreases. This leads some researchers to assume that the stages in the figure correspond to the three steps listed in the formation of a graphite spheroid. The separated graphite conical sectors indicate the beginning of the formation of degenerate graphite. As the graphite in Figure 3b was obtained from the graphite flotation zone in a large casting, it is reasonable to assume that it has grown mostly in the liquid. Pockets of iron entrapped behind the growing sectors support this supposition.

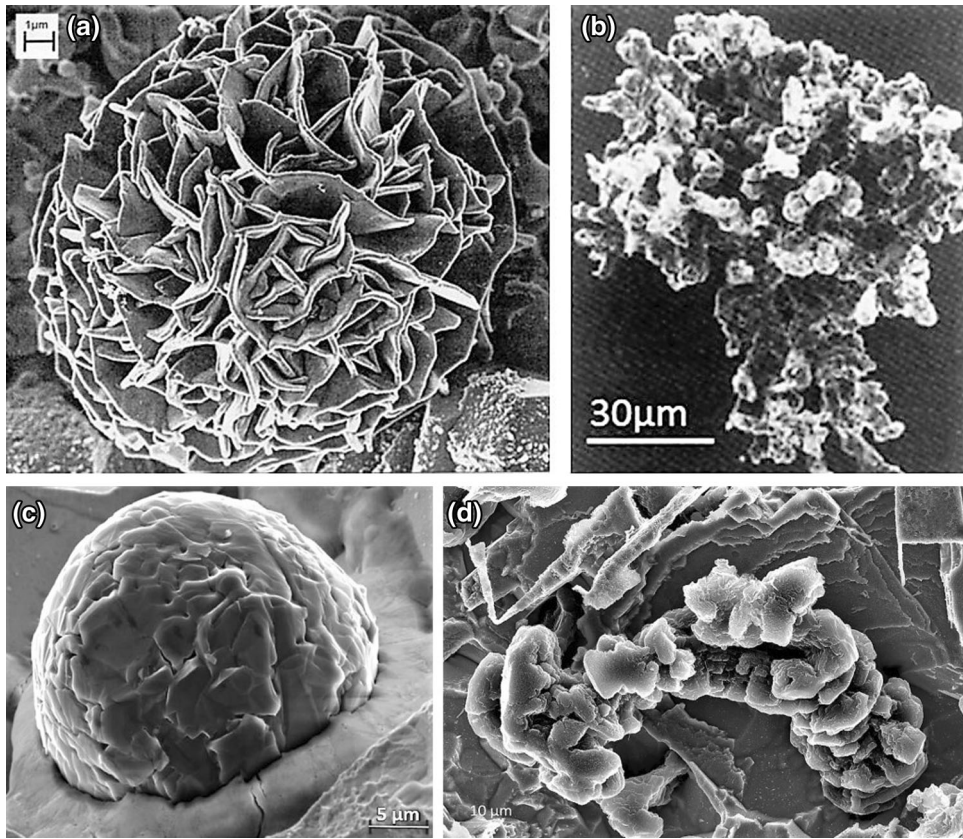


Figure 2. Typical graphite shapes found in commercial cast iron: (a) LG aggregate after deep etching;² (b) extracted CG aggregate;³ (c) SG after deep etching;⁴ (d) chunky graphite after deep etching.⁵

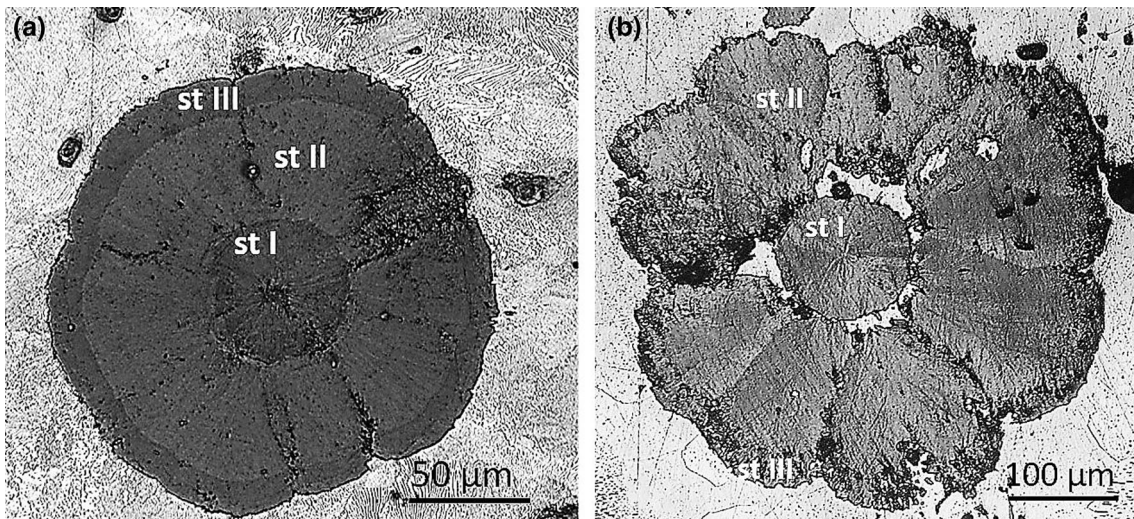


Figure 3. Three-stage graphite aggregates: (a) optical image of well-formed graphite spheroid (compliments of J. Barlow and A. Catalina, Caterpillar Inc.); (b) optical micrograph of a degenerated (exploded) graphite spheroid (compliments of A. Udroui).⁷

Crystal Growth in Systems Analogous to Cast Iron

The term “analogous systems” used in this paper is intended to describe other eutectic systems or processes that produce crystal shapes similar to that of graphite in

cast iron. They include silicon in aluminum–silicon alloys and graphite in nickel–carbon or cobalt–carbon alloys. It also includes systems that exhibit crystal shapes like that of graphite in cast iron, such as water–ice (snow crystals).

Crystallization of Silicon in Aluminum–Silicon Alloys

Silicon belongs to group 14 in the periodic table, and is listed under carbon and above germanium, tin and lead. It has a greater density in liquid state than in solid state, and it expands when freezing, like water. Silicon, like carbon and germanium, crystallizes in a face-centered diamond cubic crystal structure with a lattice spacing of 0.543 nm.⁸

Analogies between the solidification of Al–Si alloys and cast iron have been discussed by several investigators.^{9,10} At slow-rate directional solidification, eutectic silicon grows with faceted fibers (Figures 4a,b, 5a), while graphite grows as continuous laths or flakes.¹¹ In some instances, the silicon can grow as dendrites, as seen for primary silicon in Figure 4a, and for eutectic silicon in Figure 4b.

Eutectic modification through rapid cooling or chemical treatment (e.g., Sr, Na) will produce fibrous silicon (Figures 4c, 5b). Sodium modification of hypereutectic Al–Si alloys can generate dendritic (Figure 6a)¹² or spheroidal growth of silicon crystals.^{13,14} When comparing the pictures in Figure 6b and c obtained from an Al–20% Si alloy modified with large additions of sodium (250–1000 ppm), it is noticed that while the appearance of the center-cut is spheroidal, that of the off-center cut appears polygonal. Needles of the ternary compound NaAlSi₄ protrude from the spheroid.

Directional solidification experiments by Nakae and Shin¹⁵ found that Sr modification induced a change from cooperative growth of Si and Al to silicon protrusions in the melt.

Primary silicon crystals with nearly ideal octahedral shape, i.e., {111} facets, as well as with imperfect polyhedral shape, i.e., {111} and {100} faces, have been also observed in cast hypereutectic Al–Si alloys.^{12,16,17} The use of a one-

step laser powder cladding process of Al–40Si on cast aluminum–alloy substrate produced five-branch silicon particles with surrounding α -aluminum dendritic halos, as shown in Figure 7.¹⁸ Note the similarity of stellar growth with the ice crystal in Figure 16a.

Fujiwara et al.¹⁹ demonstrated that faceted dendrites can grow from Al–40 Si melts during the solidification of a laser pool. Typical growth behavior of a Si-faceted dendrite is presented in Figure 8. The dendrite grows faster than the rest of the crystal and propagates not only in the rapid-growth direction but also perpendicular to the rapid-growth direction. Growth steps are seen on the side of the dendrite. Two {111} parallel twins are observed. The growing Si dendrite rejects Al until the local concentration is sufficient to nucleate α -aluminum phase that grows as a halo around the Si particle and arrest the growth of silicon particles. The increased Si content of the remaining liquid eventually displaces the composition of the liquid in the coupled zone and cooperative growth of the Al–Si eutectic follows. During slow cooling, no twins were formed. A hexagonal crystal with 120° corners, which is the equilibrium shape of the Si crystal, was obtained.

Eutectic silicon in non-modified sand-cast Al9Si3Cu alloy solidifies as platelets,²⁰ as shown in Figure 9a. Of particular interest are the platelets in Figure 9b, which appear to be foliated dendrites. The growth mechanism of foliated crystals and dendrites which are assemblies of thin plates separated by solvent impurity layers was first postulated by Saratovkin.²¹

Crystallization of Graphite in Nickel–Carbon Alloys

Analogies between graphite morphology in Fe–C and Ni–C alloys were observed very early in the development of SG iron. Examining the structure of lamellar graphite in a

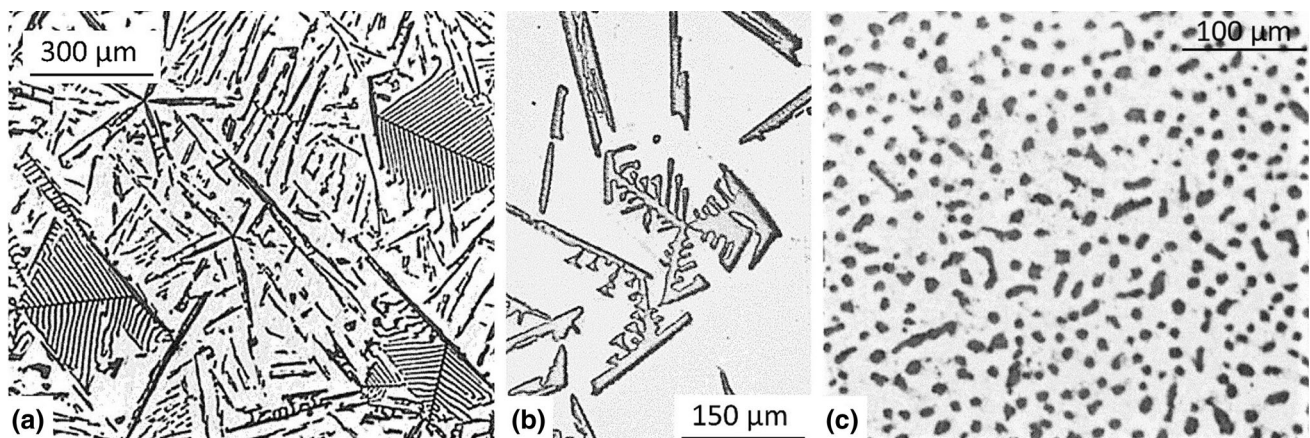


Figure 4. Optical micrographs of silicon morphologies in Al–Si alloys:¹¹ (a) eutectic silicon and complex regular and star like primary silicon in hypereutectic alloy; (b) massive faceted eutectic silicon with dendritic appearance; (c) strontium-modified fibrous silicon

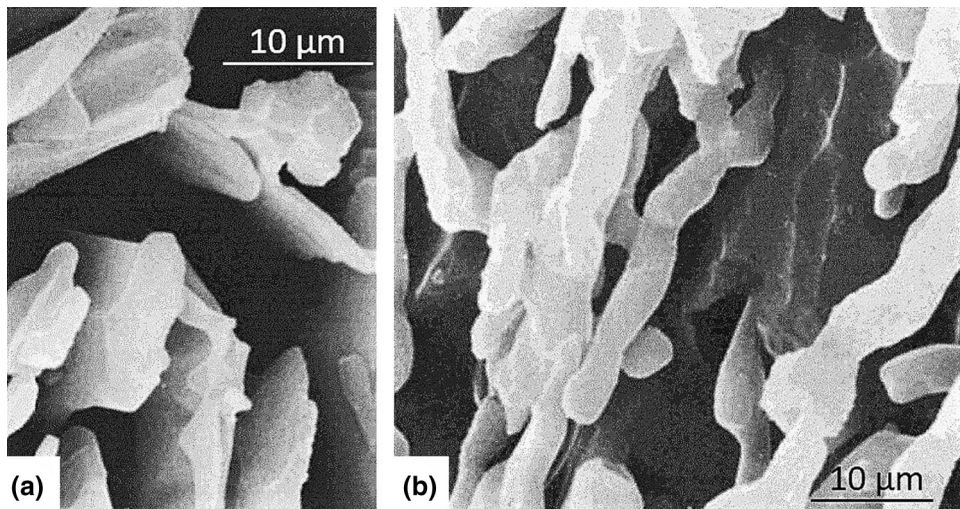


Figure 5. SEM micrographs of silicon morphologies in Al-Si alloys:¹¹ (a) flake eutectic silicon; (b) strontium modified fibrous silicon

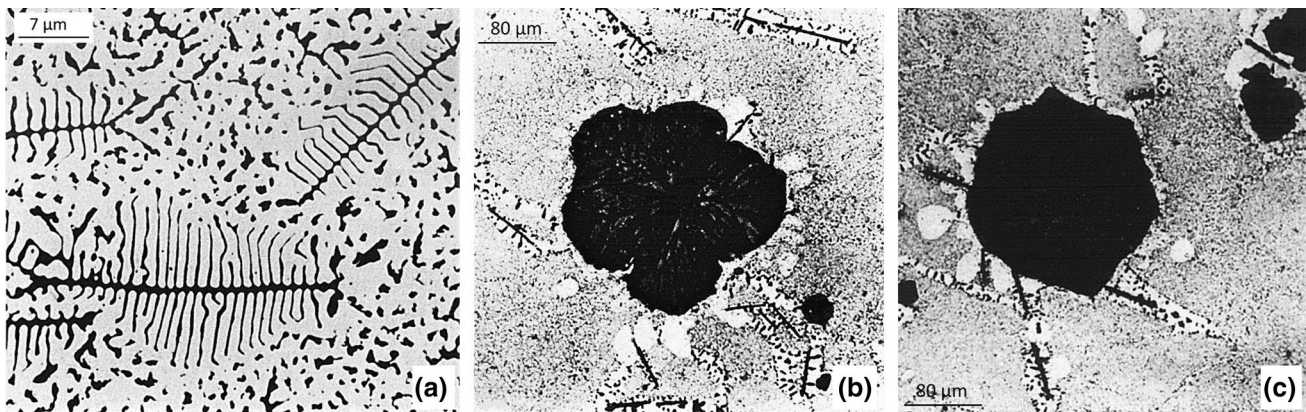


Figure 6. Optical micrographs of silicon morphologies in sodium-modified Al-Si alloys: (a) dendritic growth,¹² (b) cut through center of spheroid,¹³ (c) off-center cut of spheroid in (b)

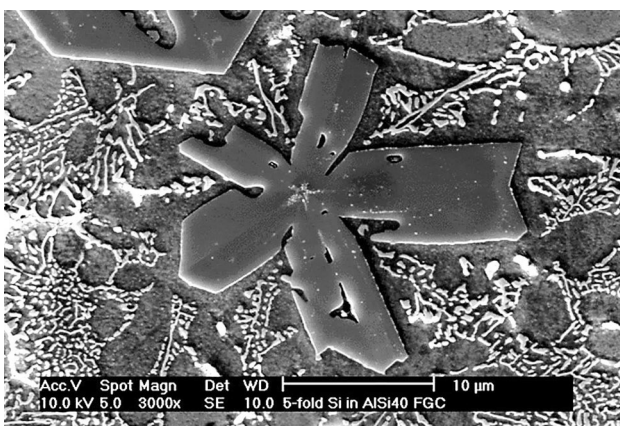


Figure 7. SEM micrograph showing the growth of a five-branch silicon crystal.¹⁸

eutectic Ni-2.1% C alloy, Double and Hellawell²² concluded that the flakes or lathes of graphite are composed of layers of fault-free crystal some 10 μm thick. Successive layers are stacked together in one of three ways, such that

they are related by rotations of $\sim 13^\circ$, $\sim 22^\circ$ or $\sim 28^\circ$ about the c -axis. Higher cooling rates may produce single fault-free sheets, and twin events during growth could then produce changes of orientation by bending of the sheet as well as branching in the plane of the crystal (Figure 10a, b).

The dendritic growth of graphite was reported as early as 1963 by Minkoff and Einbinder²³ on an imperfect graphite spheroid found in a Ni-C melt. They further argued that every branch of the dendrite may be regarded as an independent columnar crystal grown from their own nucleus situated along the principal trunk of the dendrite.

Lux et al.²⁴ have found dendritic branching of graphite primary crystals in Ni-C alloys (Figure 10c). The dendrite branches grow from the $(10\bar{1}0)$ faces. The lack of symmetry of the dendrites is attributed to the rotation boundary faults in the crystal.

Amini and Abbaschian⁴ studied the growth of graphene from molten hypereutectic Ni-3% C alloy using a

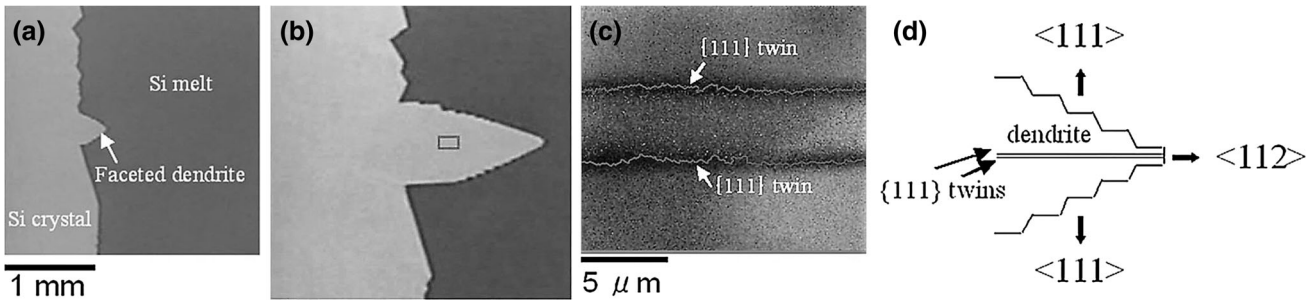


Figure 8. Silicon dendrite growth in a Al-40 Si melt:¹⁹ (a) *in situ* observation—initial stage; (b) *in situ* observation—developed dendrite; (c) EBSD analysis at box in (b); (d) orientation relationship in the faceted dendrite

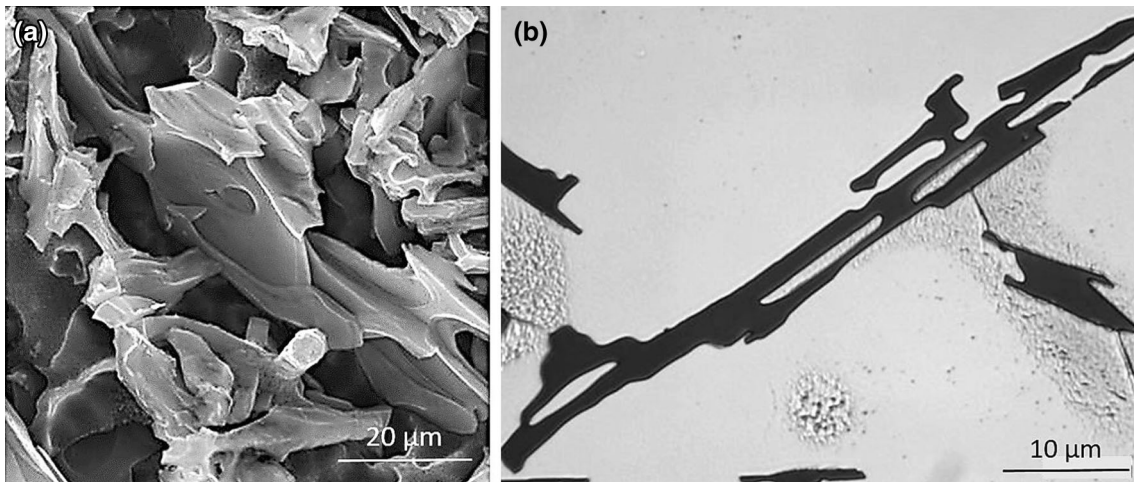


Figure 9. SEM images of eutectic silicon platelets:²⁰ a) SEM image; deep etched, HCl; b) optical image; etched, Dix-Keller; growth of protuberances between plates to produce foliated dendrites

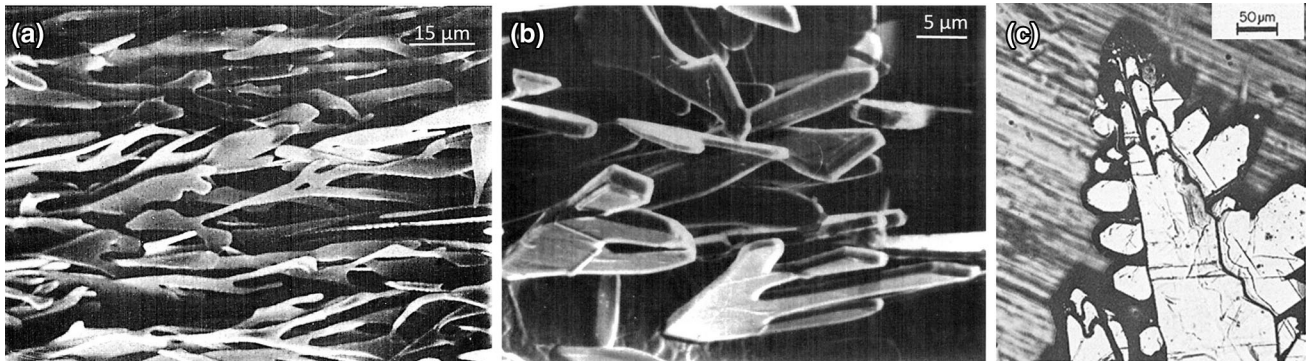


Figure 10. Micrographs of graphite lamellae in Ni-C alloys: (a) graphite lamellae in a eutectic Ni-C alloy solidified at 3.3×10^{-6} m/s; SEM micrograph;²² (b) graphite lamellae in a eutectic Ni-C alloy solidified at 2×10^{-7} m/s; SEM micrograph;²² (c) Dendritic branching of graphite; optical micrograph.²⁴

containerless melting process. They found that upon cooling of supersaturated hypereutectic alloys, primary graphite can grow either with flake or spherical morphology, depending on the solidification rate and supersaturation. At small solidification rates, the graphite crystals were bounded by faceted basal and prismatic planes (Figure 11a, b). They suggested that the growth of these faceted interfaces is by migration of the ledges produced by 2D

nucleation. As the growth rates increase, graphite interfaces become kinetically rough and the growth rate is limited by the diffusion of carbon to the growth interface. As a result, both interfaces grow with a relatively similar rate leading to initiation of graphite sphere formation.

Comparison of the images in Figures 10a and 11b suggests that the structure in the latter figure is the result of bending

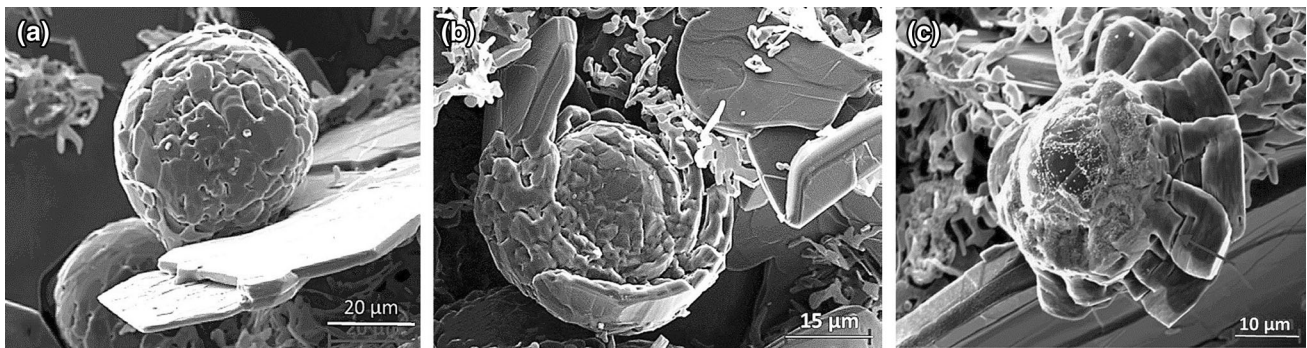


Figure 11. SEM images of graphite growing out of Ni-3% C melts:⁴ (a) spheroidal and lamellar graphite; (b) spheroidal to lamellar growth transition of graphite; (c) columnar growth

of the graphite platelets, as originally suggested by Sadocha and Gruzlesky²⁵ under the terminology “circumferential growth” or “curved crystal growth.” The lateral branching may be construed as dendritic growth of the graphite platelets. These dendrites seem to appear as crystals producing a curved tiled-roof configuration.

Growth of Other Hexagonal or Tetragonal Crystals

In this section, hexagonal ice crystals and tetragonal Al₃Ti crystals growing in aluminum–titanium alloys will be discussed.

Crystallization of Ice Crystals

Ice has a regular crystalline structure based on the molecule of water. While ice molecules can exhibit up to sixteen different packing geometries, natural ice has a hexagonal crystalline structure. The three-dimensional crystal structure of hexagonal ice is composed of H₂O molecules located on the apex of hexagons. The two-dimensional hexagonal space lattice is shown in Figure 12. The H–O–H angle is 106.6° and the O–H distance is 0.0985 nm.²⁶

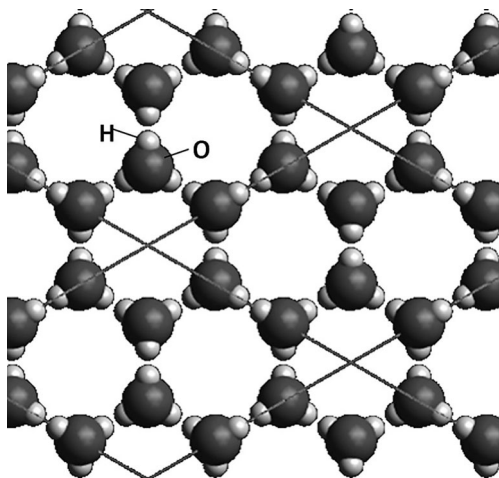


Figure 12. Two-dimensional lattice structure of hexagonal ice

Based on observations with the latest invention of the day, the microscope, Robert Hooke published in 1664 many snow crystal drawings, which for the first time revealed the complexity and intricate symmetry of snow crystal structure.²⁷ Faceted growth of snow crystals leads to a rich diversity of forms with sixfold symmetry.²⁸ Figure 13a presents a crystal with polyhedrons arranged in sectors. The begging of a pyramidal sector-to-dendrite transition appears at the lower end of the crystal in Figure 13b. Full dendrites are presented in Figure 13c.

Nakaya²⁹ suggested that the morphological stability of ice crystals is controlled by supersaturation, temperature, and crystal size. Snow crystal structures result from diffusion-limited crystal growth in the presence of anisotropic surface energy and anisotropic attachment kinetics. As seen from Figure 14, higher supersaturation (humidity) favors complex dendritic shapes, while lower supersaturation produces plates and prisms with a hexagonal habit. Similar experimental results were also obtained by Mason,³⁰ who used a nylon fiber hung vertically in a water vapor diffusion chamber with a temperature gradient imposed along the fiber. A more recent and complete classification of ice crystals was provided by Magono and Lee.³¹

Hexagonal polyhedral crystals grow in the *c*-direction by growing platelets as seen in the growth sequence in Figure 15. Then, at higher undercooling, the ice polyhedrons develop dendrites that start growing at the apexes of the hexagonal plates.³² Transitions from polyhedral to dendritic or from dendritic to polyhedral may occur, depending on local conditions. Selected SEM images of ice crystals are presented in Figure 16. It is seen that the range of ice morphologies includes polyhedral blocks, hexagonal plates/dendrites, and even spheres.

From the computational standpoint, obtaining facet growth in combination with dendritic branching is a challenging task. Barrett et al.³³ have performed numerical simulations of snow crystal growth in two and three dimensions, producing solid plates, solid prisms, hollow columns, needles, dendrites, capped columns, and scrolls on plates. A linear

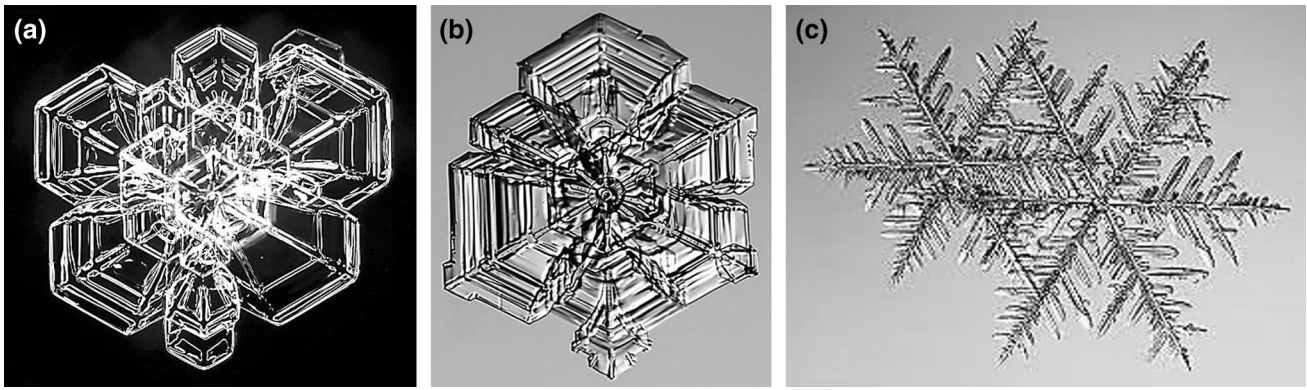


Figure 13. Optical images of snow crystals morphology:²⁸ (a) polyhedral growth of inverted pyramidal sectors; (b) polyhedral-to-dendritic transition; (c) dendritic growth

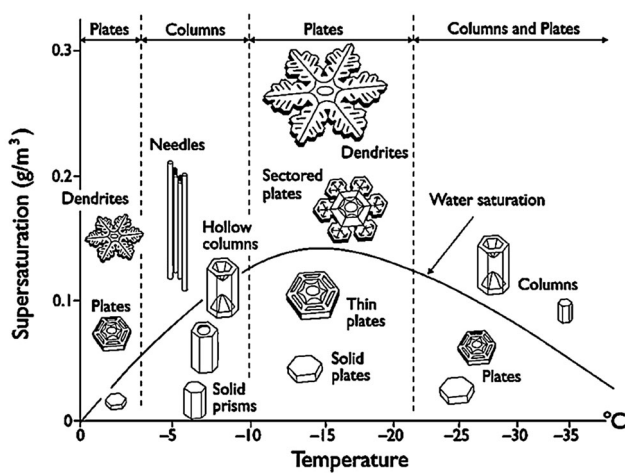


Figure 14. Nakaya diagram of structures of snow crystals.²⁹

relationship between tip velocity and supersaturation was observed. Surface energy effects, although small, had a pronounced effect on crystal growth.

The main difference between snow crystals and graphite consists in the twinning tendency of the graphite hexagonal platelets.

Crystallization of Al₃Ti in Aluminum–Titanium Alloys

Foliated dendrite growth was observed in other metallic alloys such as an Al–Ti alloy, where the faceted Al₃Ti

phase developed into “tiled-roof” structure.³⁴ The faceting is affected by composition and processing parameters. In Figure 17a, it is seen that only major faceting occurs on the (001) plane. Tiled-roof structures are shown in Figure 17b, c.

Growth of Graphite Through Other Processes

In this section, we will discuss metamorphic graphite, and graphite produced through gas-to-solid and solid-to-solid transformation.

Crystallization of Metamorphic Graphite

Metamorphic graphite is natural graphite formed through transformation by heat, pressure, or other natural actions.

Kvasnitsa et al.³⁵ have provided a complete series of crystal morphologies for natural graphite, from plate, to columnar, to pseudo-bipyramidal (two pyramids symmetrically placed base-to-base) and pseudo-bipyramidal-prismatic, to nearly spherical, which appears to have been deposited from a carbon-rich fluid. Graphite crystals were isolated from the anorthosite rock by chemical decomposition using hot HCl and HF and examined by SEM. Most of the graphite crystals show the typical graphite (0001) layered growth, without visible evidence of dislocations. In the crystals in Figure 18, straight macro-steps originate at or near the center of the polyhedron faces, and in some

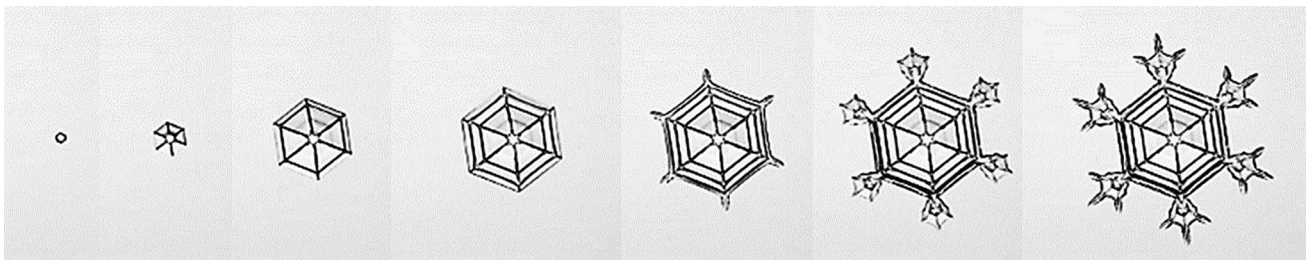


Figure 15. Development of an ice dendrite; undercooling increases from left to right.³²

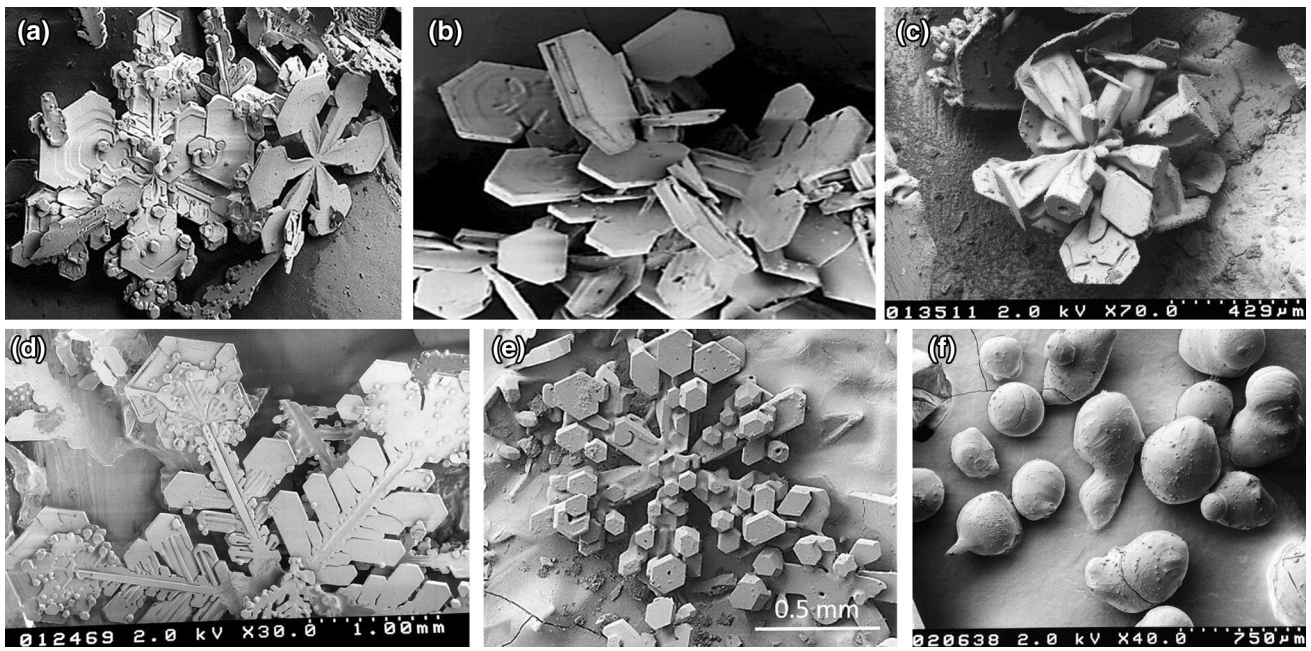


Figure 16. Low-temperature SEM images of ice crystals [Beltsville Agricultural Research Center]: (a) mixtures of polyhedron/plate and dendritic ice crystals; (b) plates growing in multiple directions; (c) columns and plates growing from a common center; (d) dendrite with polyhedron ends; (e) ice dendrite with polyhedral outgrowths; (f) spherical crystals of artificial snow (probably from remelting)

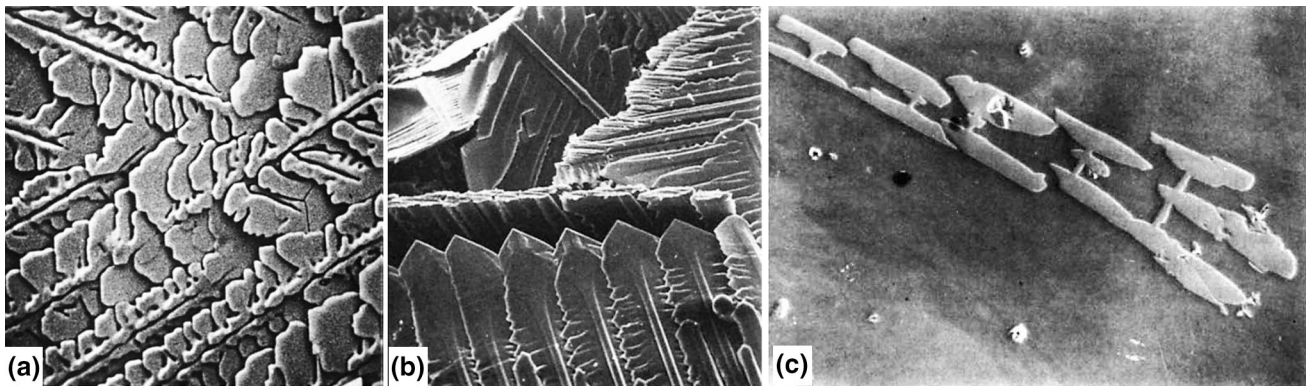


Figure 17. Foliated layers of Al_3Ti in aluminum–titanium alloys:³⁴ (a) Al–5wt% Ti alloy; $V = 1090 \mu\text{m/s}$, $G = 255 \text{ }^\circ\text{C/cm}$; $\times 400$; (b) tiled-roof structure on primary and secondary arms of an Al–2wt% Ti; $V = 87 \mu\text{m/s}$, $G = 200 \text{ }^\circ\text{C/cm}$; $\times 240$; (c) section through thickness of a dendrite in a Al–1.15wt% Ti alloy showing several foliated layers; $V = 20 \mu\text{m/s}$, $G = 200 \text{ }^\circ\text{C/cm}$; $\times 40$

cases, appear as overlapping segments from a single crystal. Because of the flexibility of the graphene sheets, the growing segments do not need to close the hexagonal pattern, but can rotate with respect to each other and overlap. As discussed by Double and Hellawell^{22,36,59} and Amelinckx et al.³⁷ such a rotation introduces another class of crystal defects, disclinations, which can promote unusual growth forms.

Thicker crystals appear to be polygonized into separate blocks of individual crystallites (Figures 18c, 19), in some cases leaving hexagonal cavities (Figure 18b) on the overall crystal aggregate. The proposed growth mechanism in Figure 19c shows early-stage helical growth (called

macro-spiral growth by Kvasnitsa) of (0001) layers, with subsequent growth of polyhedral blocks. The polygonized growth is shown taking place around the central macro-spiral every 120° .

Thicker polygonized blocks of crystals show a deviation from parallelism of the (0001) planes, and their predominance leads to the formation of more unusual pseudo-bipyramidal and pseudo-bipyramidal-prismatic aggregates (Figure 19a, b). More dramatic splitting of the overall aggregate into individual crystallites was also observed (Figure 20a). Polyhedral growth and the deviation of parallelism of the crystallite blocks may result in nearly spherical aggregates (Figure 20b), various bipyramidal-

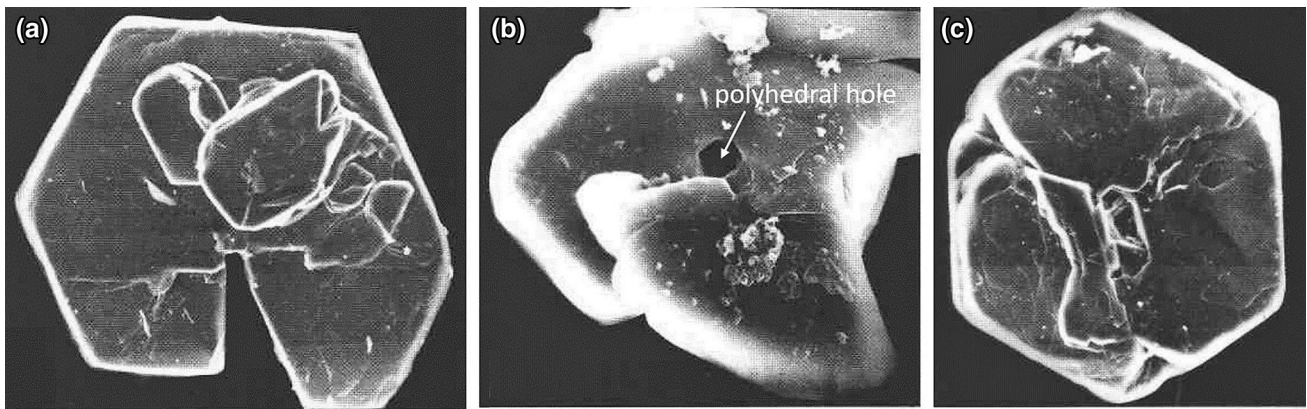


Figure 18. Plate graphite crystals showing various stages of micro-spiral growth. Crystal sizes range from 0.2 to 0.5 mm across:³⁵ (a) beginning of helical growth; (b) helical growth producing polyhedral hole; (c) polygonization into blocks

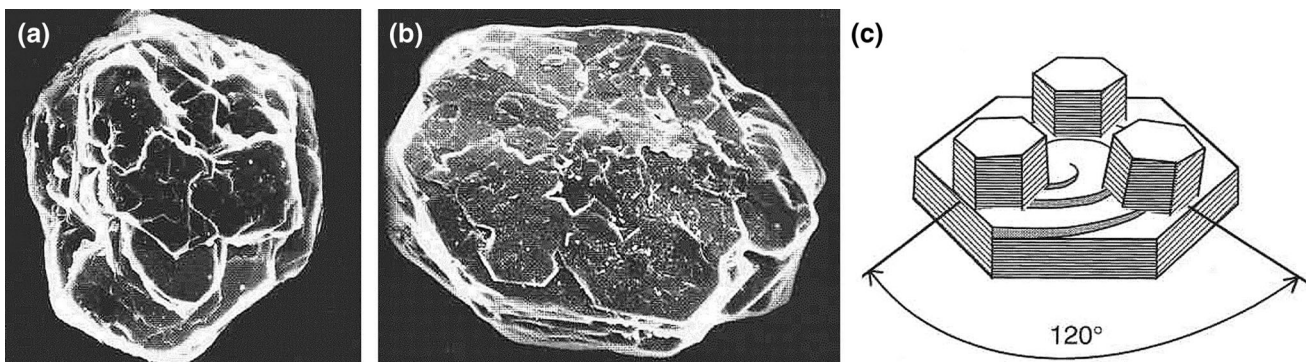


Figure 19. Metamorphic graphite blocks:³⁵ (a) formation of separate polygonized blocks around the macro-spiral; (b) formation of pseudo-hexagonal bipyramids; (c) proposed mechanism

prismatic crystal forms (Figure 20c), and even columnar morphologies (Figure 21). Several of the columns in Figure 21 originate from the central column. They seem to grow at an angle with respect to the orientation of the central column.

It was suggested³⁵ that early-stage micro-spiral growth with the introduction of a negative wedge disclination is

conducive to the bending of the graphene sheets and to polygonization. Cavities would be expected at the centers of the plate crystals because of the high strain from the disclination and the macro-step formation. After further growth and polygonization, the cavities would become concealed. The bending of the graphene sheets induced by the disclination could lower the overall symmetry of the aggregate from sixfold to threefold (hypomorphism),

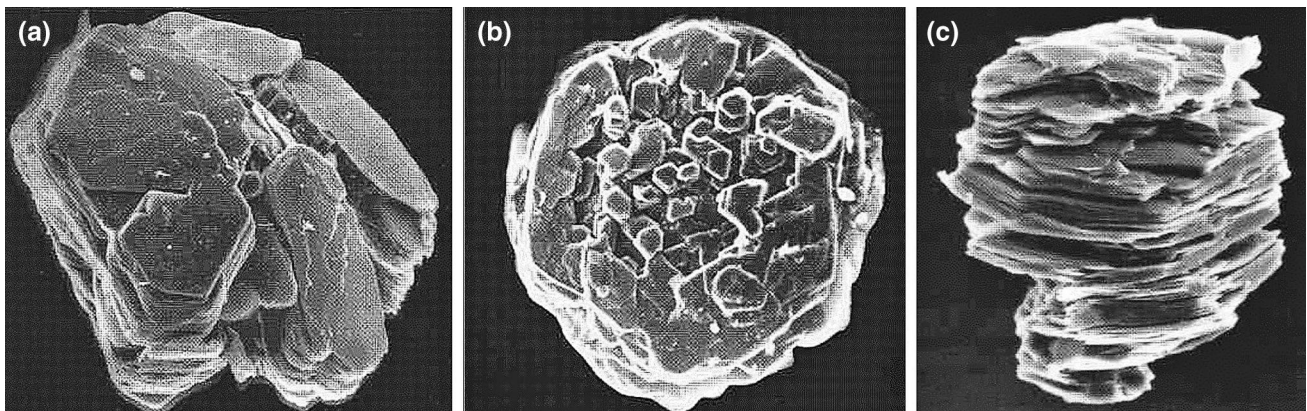


Figure 20. Other forms of metamorphic graphite:³⁵ (a) splitting of the crystal into separate pinacoidal or pinacoidal-prismatic blocks; (b) early spherical graphite aggregate; (c) pseudo-bipyramidal-prismatic crystal showing bending in the platelets

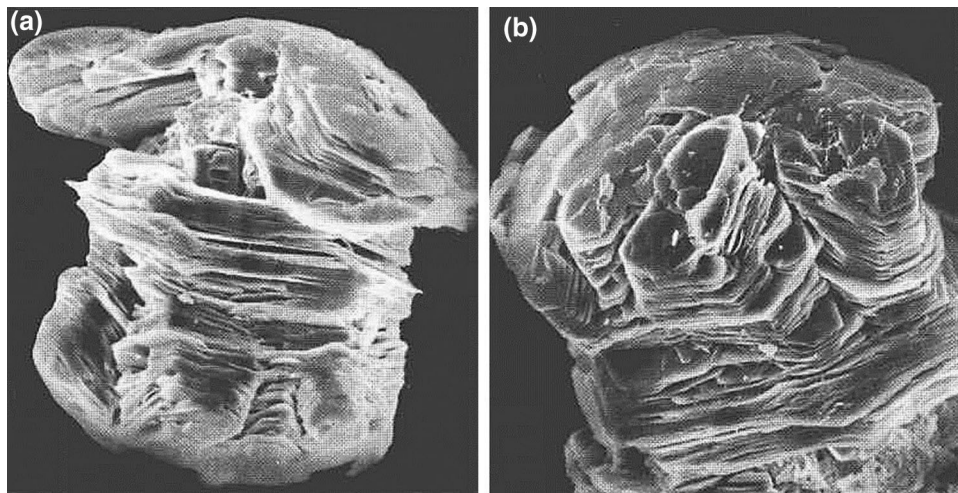


Figure 21. Columnar forms of metamorphic graphite.³⁵

which explains the rounding of the platelets seen in Figure 21. During the growth of the micro-spiral, the bending of the sheets will produce increasing lattice strain. At some critical thickness, this elastic energy will become too large, and polygonization would be expected to take place, leading to formation of separate crystallites slightly misoriented with respect to each other. Subsequent growth would lead to a pseudo-bipyramidal-prismatic morphology.

Growth in the *c*-direction can also be explained through the twist-tilt boundary mechanism suggested by Frank.³⁸ Small angle tilt or twist boundaries between adjacent grains of graphite provide nucleation sites for growth along the *c*-axis. Some evidence for this growth mechanism can be seen from the arrangement of steps on the pinacoid surfaces in Figure 20a.

Jaszczaka et al.³⁹ reported on the finding of cones formed from a metamorphic fluid on the surfaces of millimeter-sized polycrystalline spheroidal graphite, extracted from calcite boudins. Sharp or rounded cones, with heights ranging from less than a micron to 40 mm were found (Figure 22a). The most common apex angle is 60°. Steps on the cone surfaces (Figure 22b) are an indication of a layer growth mechanism, suggestive of growth in a fluid rather than from solid-state transformation of carbonaceous sediments. Convergent beam electron diffraction patterns from a single cone are also consistent with the graphene sheets lying parallel to the cone surface. The natural cones have a wide distribution of apex angles, which supports a disclination model for cone-helix structures.

An alternative model for the generation of cones is the occurrence of pentagonal defects in the graphene structure, which will result in the bending of the sheet with formation of an apex (Figure 22c). However, the consistency of the cone-helix model with observed apex angle distributions suggests that the nucleation of pentagon defects is not the only factor determining graphite cone morphologies, but

that the energetics of layer-layer interactions between the graphene sheets is also a factor.

Graphite Produced Through Gas-to-Solid Transformation

Chemical vapor deposition processes have been used to generate pyrolytic graphite sphere (PGS). Recent work by Li et al.⁴⁰ demonstrated that graphite spheres obtained from gas-solid transformation has similar structure of radial sectors in the cross section as the spheroidal graphite (SG) in steel grown through solid-solid transformation, as well as the SG in ductile iron from liquid-solid transformation (Figure 23a). The plasmon ratio image of energy-filtered TEM images that can reflect the graphitic degree of carbon materials⁴¹ shows that the periphery of a PGS section has a higher graphitic degree than the central region.

The high-resolution TEM (HRTEM) analysis of 002 fringes of a PGS in Figure 23b shows that the fringes in each sector are mostly parallel straight lines, indicating a high degree of graphitization near the periphery of the PGS. The interplanar spacing in the high graphitic areas is about 0.345 nm. The grain boundaries in the PGS are either coherent at small angles, as in position *d* at 13°, or incoherent at large angles, as in position *c* at 40°. The incoherent 40° boundary contains many defects. Low graphitic domains are seen in position *e* where the fringes change directions. The low graphitic core is attributed to growth on droplets that serve as nuclei. At later growth stage, the dominant mechanism is absorption that produces the high graphitic periphery.

Yoon et al.⁴² obtained platelet-type, herringbone-type, and tubular-type carbon nano-fibers through catalytic routes. Using SEM, TEM, STM, and XRD, these nano-fibers were found to have common substructures, which were termed carbon nano-rods (CNR) and carbon nano-plates (CNP).

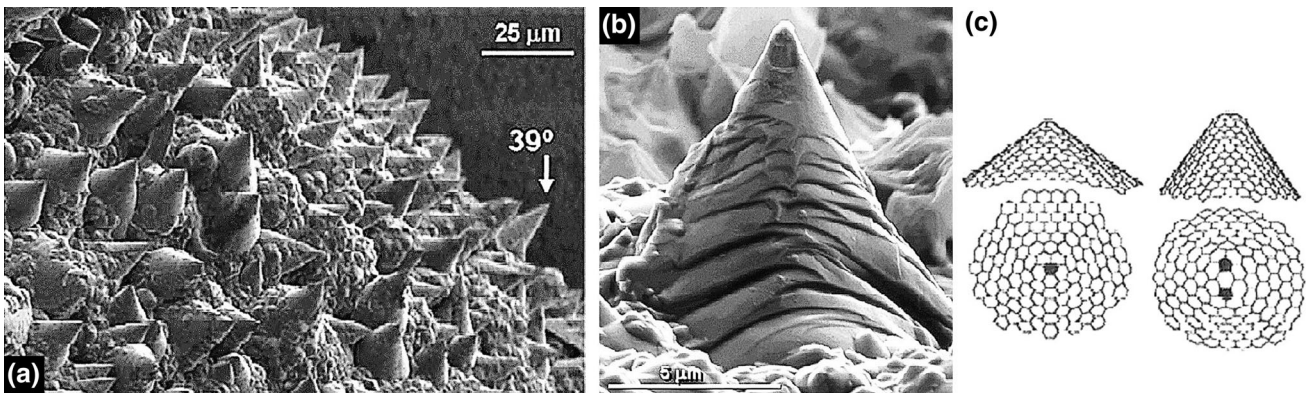


Figure 22. Graphite cones on a quasi-spherical metamorphic graphite:³⁹ (a) graphite cones; (b) higher magnification of (a); (c) possible model for cone growth

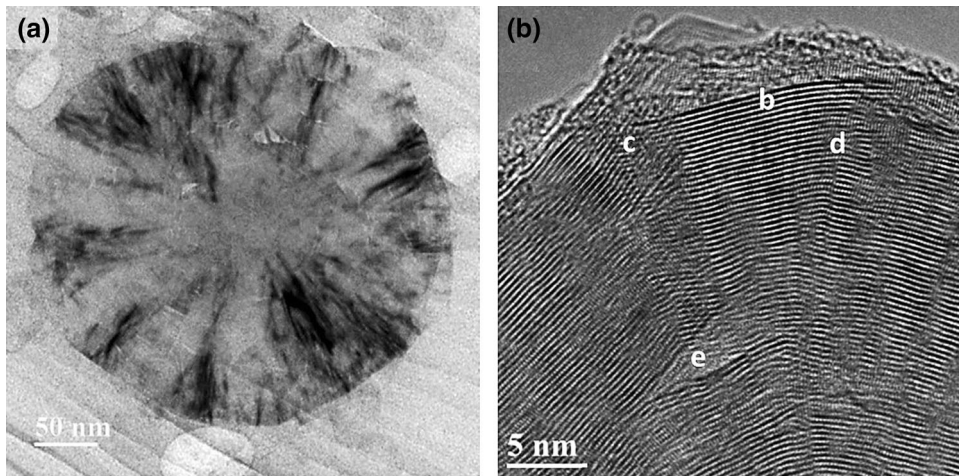


Figure 23. TEM images of pyrolytic graphite spheres:⁴⁰ (a) cross-sectional image of a PGS; (b) HRTEM image of 002 fringes of a PGS

A CNR was a carbon cluster of 8–10 graphene layers with unique diameters of about 2.5 nm and lengths of 15–100 nm. CNPs appeared to be sets of 5–25 graphene stacks, probably formed by association of several CNRs. The faceted catalyst surfaces determine the particular ordered arrangements of the CNRs or CNPs in the final fiber form that result in the production of platelet, herringbone, or tubular-type nano-fibers (Figure 24).

Graphite Produced Through Solid–Solid Transformation

In iron–carbon alloys, graphite also precipitates through a solid–solid transformation. Indeed, during further cooling after solidification, the solubility of carbon in austenite decreases, which generates some C diffusion from the austenite to the graphite. This diffusion also occurs during the austenite-to-ferrite and/or pearlite transformation. This will be further discussed in the section solidification of spheroidal graphite (SG), later in this paper.

What is of interest in this section is the formation of new graphite through solid–solid transformation. Typical cases

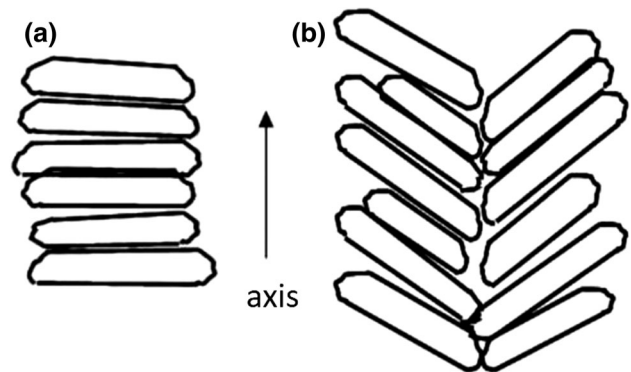


Figure 24. Stacking of hexagonal plate units in carbon nano-fibers:⁴² (a) platelet-type; (b) herringbone-type

include annealing of white iron to produce malleable iron and heat treatment of carbon steel.

The graphite in malleable iron is termed temper graphite. Its morphology ranges from irregularly shaped nodules to spheroidal. Spheroidal graphite is obtained when the iron was treated with Mg or when the Mn/S ratio is smaller than

one. In this latter case, the spheroidizing effect appears to be connected to the type of inclusions in the iron, which are predominantly (MnFe)S at Mn/S < 1, and MnS at ratios Mn/S > 1.7.⁴³ Also, it is well known that adding Mg to the low carbon equivalent liquid iron that solidifies white produces spheroidal graphite in the annealed structure.

He et al.⁴⁴ examined 2–5- μm graphite nodules found in 0.38% carbon steel quenched to martensite and then annealed for 2 h. Some of the graphite nodules had an irregular morphology and a nucleus (nitride or oxide), while others were more regularly spheroidal with no apparent nucleus. The structure of the small spheroidal nodules suggested a regular radial growth mechanism of conical sectors radiating from the central region, with an increasing level of orderly arrangement of the graphene layers, beginning from a more disordered arrangement, or amorphous carbon center (Figure 25). The authors suggested that the mechanism is similar to the cone-helix growth mechanism of Double and Hellowell³⁶ for nodular graphite forming from supersaturated liquid melt in Fe–C or Ni–C alloys, also supported by a study by Miao et al.⁴⁵ The main difference is that while the Double/Hellowell mechanism assumes helical growth of the graphite platelets, the He et al. mechanism assumes growth in the *c*-direction through spiral growth. These authors further suggested that the amorphous center could be associated with carbon-rich amorphous regions connected with the partially dissolved initial carbide particles that form from the quenched martensite during the early stages of annealing. This hypothesis was confirmed in subsequent work.⁴⁶ A more recent study of SG obtained by heat treatment of medium carbon steel by Li et al.⁴⁰ also concluded that the graphite aggregate is built of radial sectors and that the building blocks of the sectors are graphite platelets (Figure 26). The platelets are about 10–30 nm thick and hundreds of nanometers in length, and grow

nearly parallel, with misorientation of up to 20°. The sectors in the TEM images can be 2D projections of 3D cones or polyhedrons.

In graphite with AlN nuclei, the graphene layers grow on the AlN nuclei at different angles (35°, 40°, and 90°), and not necessarily parallel to the graphite/AlN interface. This implies that the shape of the SG growing on a nucleus, which is more irregular than that of SG without visible nucleus, is influenced by the inclusion shape.⁴⁰

Li et al. argue that the growth at initial stage is kinetically controlled. Otherwise, the core will be polyhedral single crystal with its shape following the Wulff construction.⁴⁰ The lengthening in *a*-direction is constrained by multiple site nucleation because the patches grown from nuclei impinge each other. The basal plane can still extend in the *c*-direction by 2D nucleation and the patches grow into radial cones. The authors further argue that the layer-by-layer thickening by 2D nucleation on basal plane supports the modified version of the cone-helix model, although their picture (Figure 46a) suggest spiral dislocation rather than helical growth.

Crystallization of Carbon in Fe–C and Fe–C–Si Alloys

Interrupted solidification experiments revealed that the basic building blocks of the graphite aggregates are hexagonal faceted graphite platelets with nanometer height in the *c*-direction and micrometer width in the *a*-direction.⁵

Such plates are shown in Figure 27a, which also reveals that thickening of the platelets occurs through growth of additional graphene layers nucleated at the ledges of the graphite prism. However, thickening of the graphite

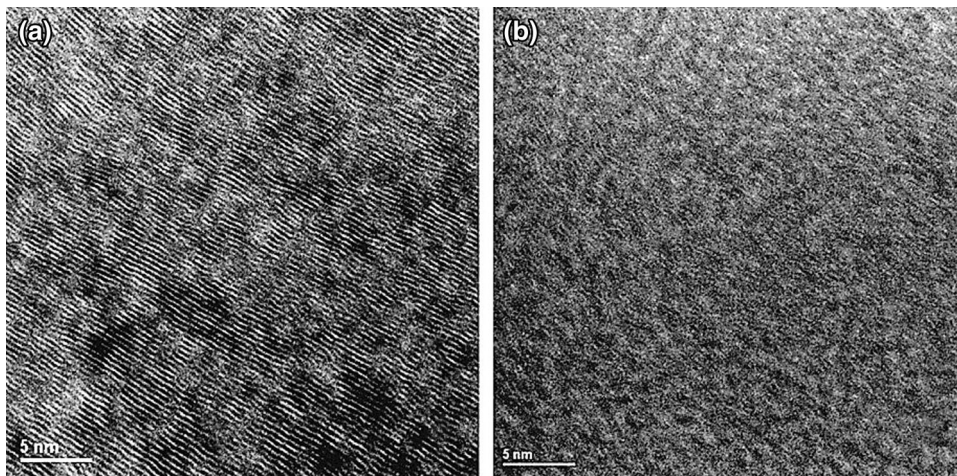


Figure 25. HRTEM images from different regions of a graphite spheroid:⁴⁴ (a) near the edge; (b) near the center

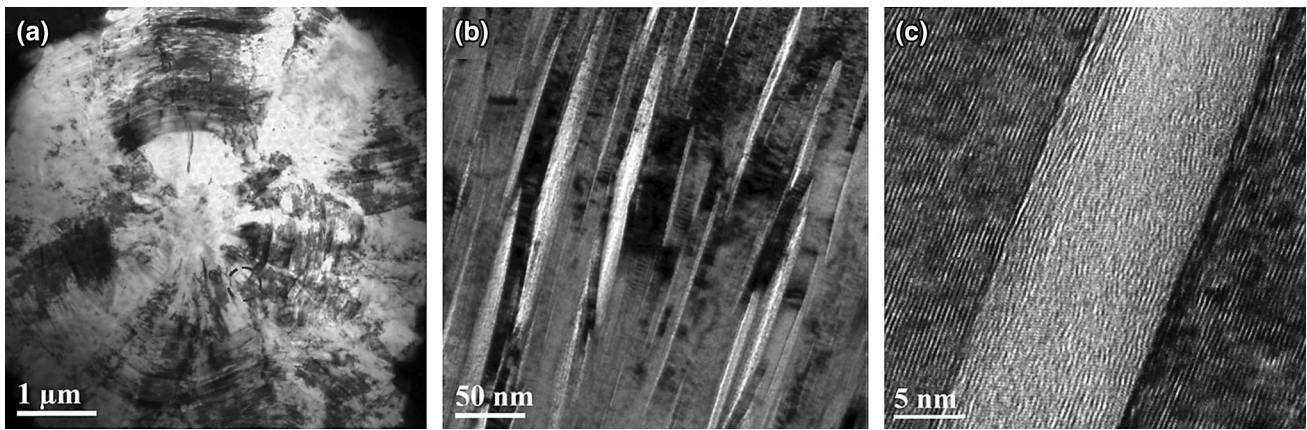


Figure 26. TEM images of a graphite spheroids obtained from a carbon steel:⁴⁰ (a) TEM image showing sectors in a SG; (b) TEM images showing graphite platelets in a sector; (c) HRTEM image showing (002) fringes of the graphite platelets

platelets may also occur through spiral dislocation growth. Examples of spiral growth of graphite can be found in both LG and CG as shown in Figure 27b, c.^{47,48}

Solidification of Lamellar Graphite (LG)

Dendritic branching in lamellar graphite has been described by Lux et al.²⁴ As seen in Figure 28, the eutectic crystals of graphite branch out of lamellar edges. The branches bend and overlap the original graphite plate.

The SEM analysis of deep-etched interrupted solidification hypoeutectic samples shows that in the initial stage lamellar graphite grows from the liquid, at the γ/L interface, as crystalline hexagonal parallel platelets, with growth morphology consistent with that of foliated dendrites (Figure 29a). The platelets then may stack into curved plates (lamellae) that grow radially from a common center, as shown in Figure 29b. The overall aspect is that of a rosette dendrite, although in classic solidification the graphite aggregate is considered to be the product of cooperative eutectic growth. In later stages, the foliated dendrite grows in layered faceted crystals with a tiled-roof

configuration (Figure 30a, b). Such tiled-roof configuration of the graphite platelets was also observed in earlier SEM and TEM work on fractured graphite lamellae as summarized in Figure 30c, d.⁴⁹

Early TEM work on lamellar graphite⁴⁹ concluded that the graphite lamellae have a layered crystal structure (Figure 31a). More recent TEM work by Hara et al.⁵⁰ also concluded that the internal structure of flake graphite consisted of thin layers of graphite and crystalline platelets arranged in a “mosaic-like” structure, which is the tiled-roof configuration discussed earlier. A clear orientation mismatch is seen on a graphite lamella in the region where the graphite plate changes direction (Figure 31b).

Solidification of Compacted Graphite (CG)

Additions of Mg or Ce increasingly change the crystallization pattern of graphite with the addition level. SEM analysis of interrupted solidification experiments of low-magnesium iron (0.013–0.02% Mg) reveals a gradual change from stacking of platelets along the *a*-direction in the tiled-roof configuration, to stacking in the *c*-direction.

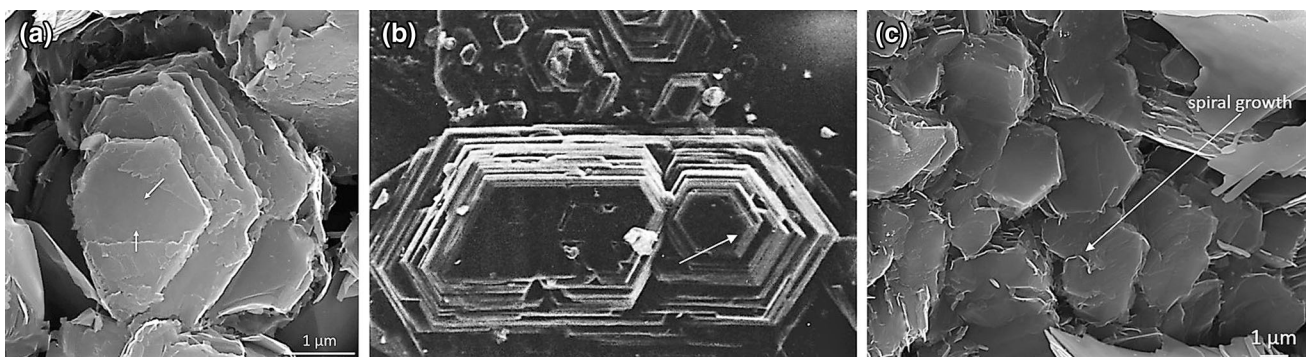


Figure 27. Examples of thickening of graphite crystals through various mechanisms: (a) growth front of new graphene layers in a CG iron sample; the arrows indicate the direction of growth of graphene layers;⁵ (b) spiral growth on kish graphite in hypereutectic LG iron;⁴⁷ (c) micro-spiral growth in CG.⁴⁸

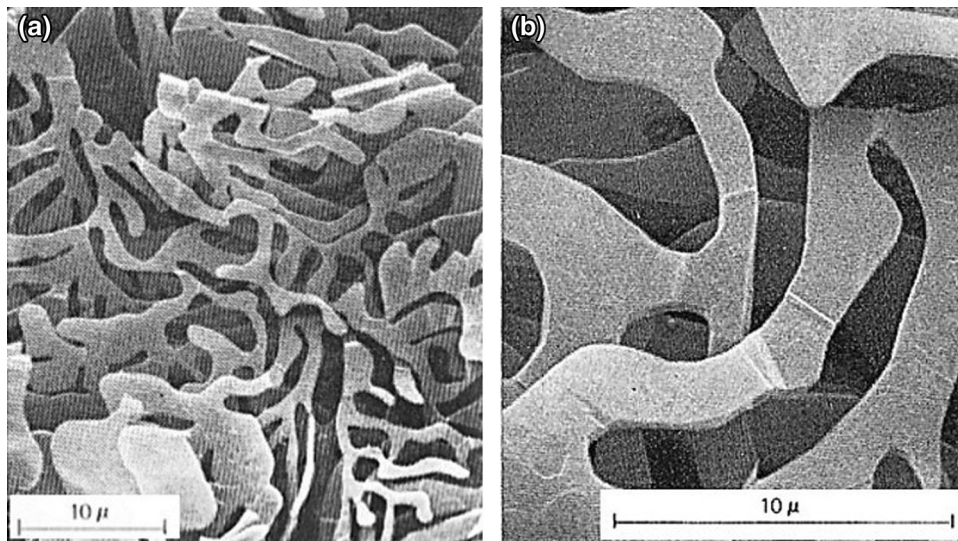
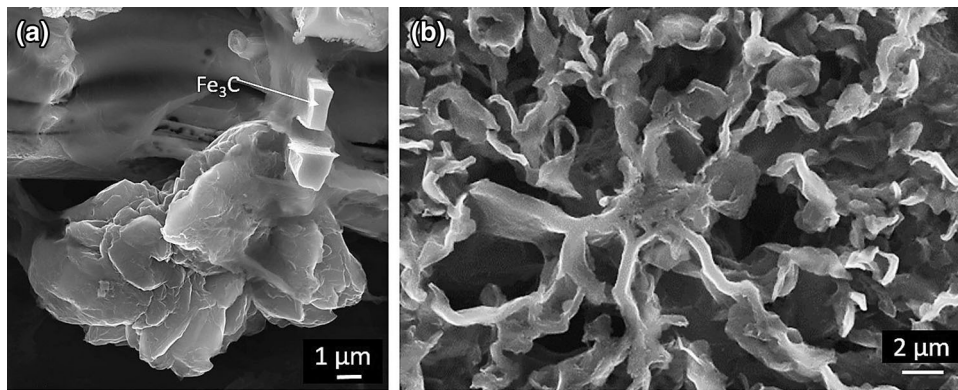


Figure 28. Dendritic branching in flake graphite normal to the c -axis:²⁴ (a) SEM image; (b) magnification of SEM image in (a)



**Figure 29. SEM images of interrupted solidification of low-sulfur LG iron:⁵ (a) stack-
ing of foliated dendrites; (b) radial growth of graphite lamellae**

Figure 32a exhibits a tadpole graphite constructed of c -direction stacked platelets. Further branching of the graphite dendrite will produce compacted graphite (Figure 32b). Stacking of the platelets in columnar structures, as in Figure 32c, may produce graphite similar to chunky graphite. The hexagonal shape of the platelets is less regular, indicating a roughening of the interface produced by the higher constitutional undercooling induced by Mg.

A clear dendritic growth pattern was found in an CG iron alloyed with antimony (Figure 33a, b). The graphite platelets stacked predominantly along the c -axis, producing clusters of blocky, rhombohedral appearance and even columnar growth (Figure 33c). The rhombohedral clusters are oriented at various angles with respect to one another. This is typical for compacted graphite irons and tadpole graphite, in which the platelets spread in the a -direction and stack in the c -direction significantly more than for lamellar graphite iron, which explains the coarser

appearance of CG as compared to LG on standard metallographic pictures.

TEM work presented in Figure 34a indicates that the morphology of CG includes graphite plates exhibiting branching and bending. Graphite platelets stacking in the [0001] direction, producing columnar blocks and curved growth of the graphite platelets is shown in Figure 34b.

Hara et al.⁵⁰ confirmed through TEM work that compacted/vermicular graphite is an aggregation of particles with a complex structure, consisting of large polygonal crystals arranged in a mosaic-like structure. We note that the micrograph in the paper shows the graphite to be poor nodularity aggregate rather than “vermicular.”

Solidification of Coral Graphite

According to Lux,^{51,52} in high-purity Fe–C–Si alloys it is possible to obtain a highly branched fibrous form of

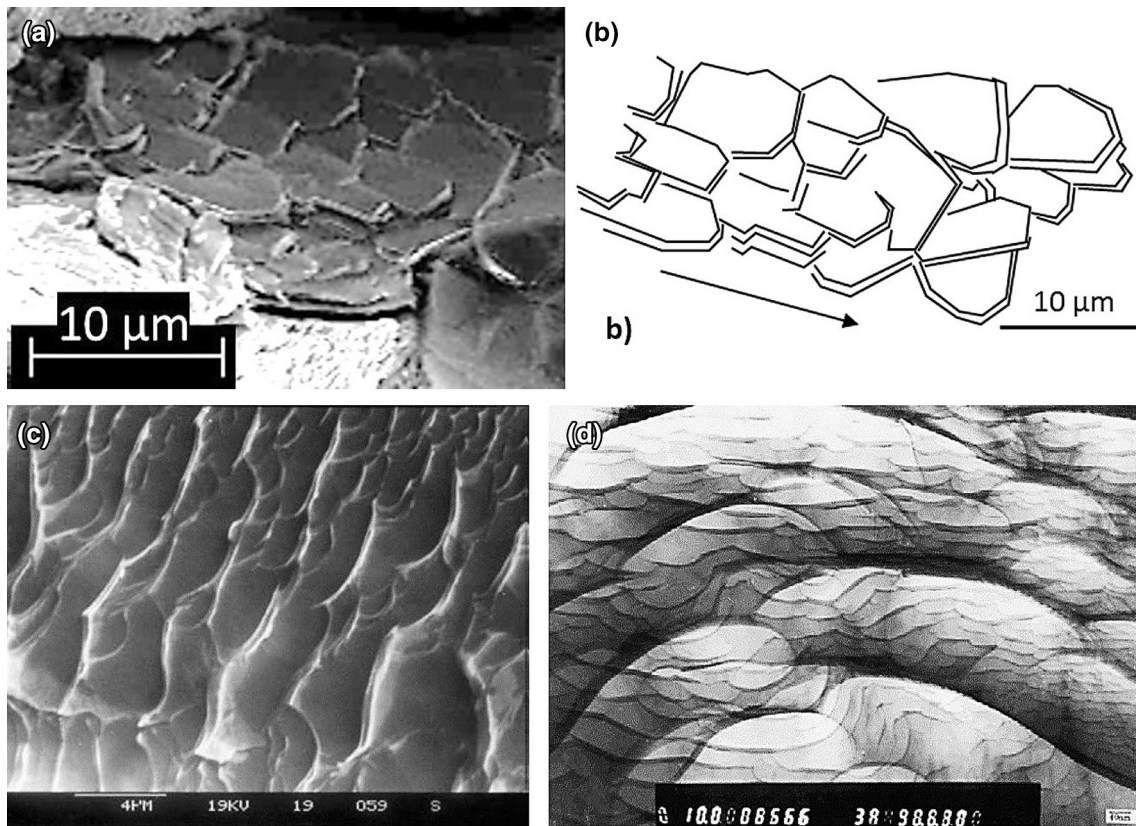


Figure 30. Tiled-roof configurations of graphite lamellae: (a) SEM micrograph of fracture area in fatigue fractured lamellar graphite iron. Compliments of W.L. Guessser and the Tupy/SENAI project; (b) drawing of lamellar graphite aggregate based on the SEM image in (a); faceted tiled-roof crystals;⁵ (c) SEM micrograph of deep-etched fractured graphite lamella;⁴⁹ (d) TEM micrograph of flake graphite.⁴⁹

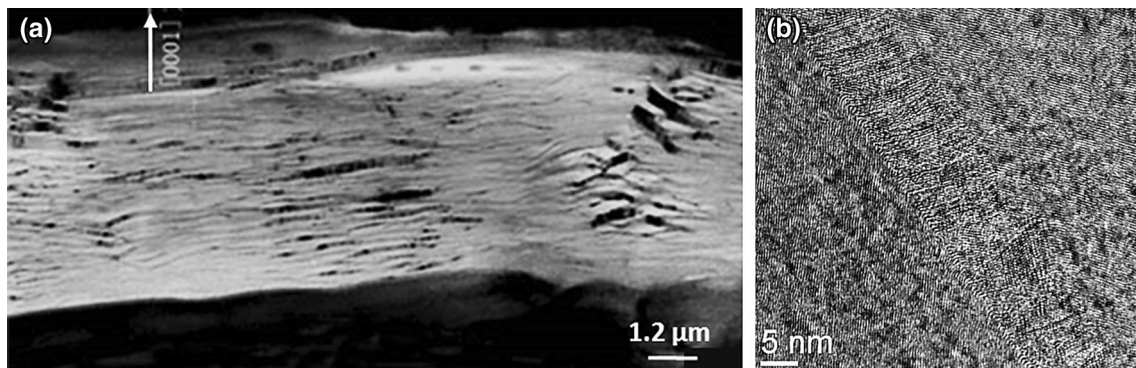


Figure 31. TEM micrographs of graphite lamellae: (a) layered graphite crystal;⁴⁹ (b) lattice fringe image of an area of orientation change inside a flake graphite.⁶⁰

graphite with fewer interconnection than type-D graphite, and more rounded edges (Figure 35). Curved plates in a tiled-roof configuration are seen on the higher-magnification pictures.

Solidification of Spheroidal Graphite (SG)

Sadocha and Gruzleski²⁵ and then Dhindaw and Verhoeven⁵³ studied the solidification of high-purity Fe-C-Si

alloys and concluded that, with increasing purity and solidification rate, a transition from plate-like or coral to spheroidal graphite occurs. SEM examination of deep-etched transition regions revealed that what appeared to be nodules in optical micrographs were, in fact, cylindrical columns of graphite, as seen in Figure 36. Nucleation of coral graphite occurred consistently around 1151 °C, irrespective of iron purity. It was argued that coral graphite formation is less sensitive to nucleation rate than SG

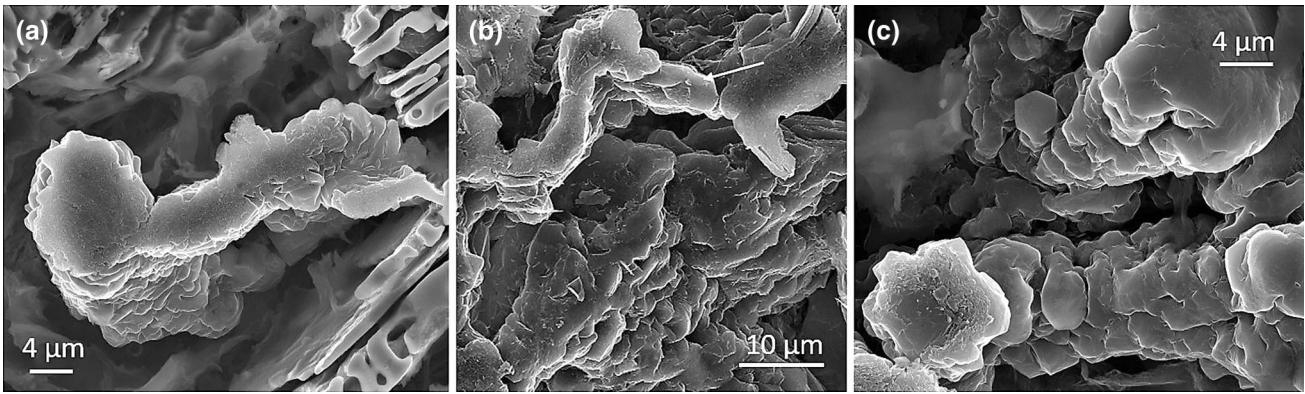


Figure 32. Stacking of graphite plates along the *c*-direction to produce various forms of graphite.⁵ (a) tadpole graphite; (b) compacted graphite; (c) chunky graphite

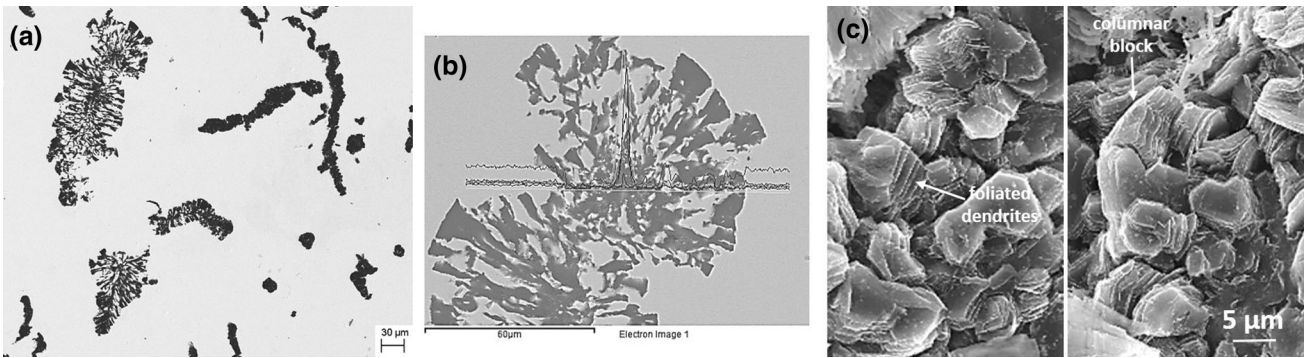


Figure 33. Microstructures of a sand-cast 0.01% Sb CG iron showing dendritic growth of graphite and stacking of graphite platelets: (a) optical micrograph; graphite dendrite;⁴⁸ (b) SEM image of a graphite dendrite;⁴⁸ (c) SEM image; stacking of foliated dendrite into polyhedral blocks

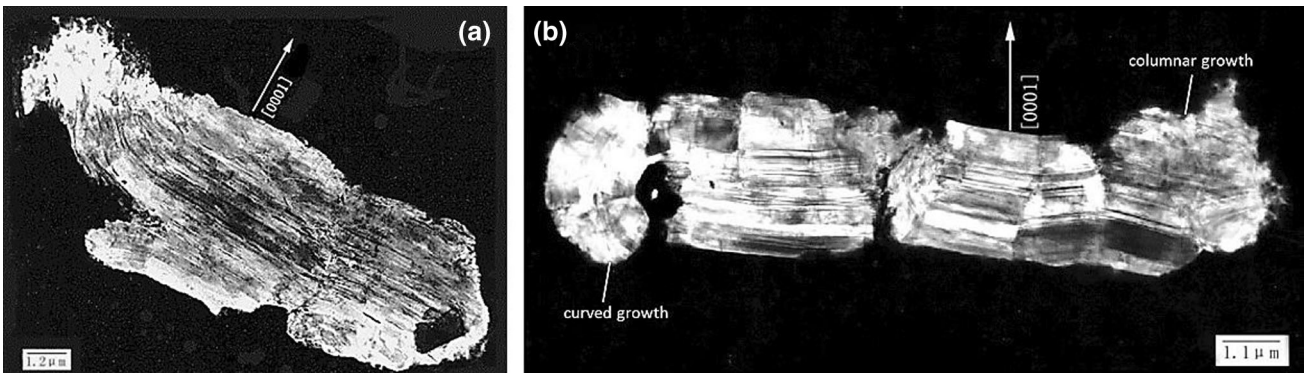


Figure 34. TEM images of extracted compacted graphite:⁴⁹ (a) branching and bending of CG aggregate; (b) curved and columnar growth of graphite platelets

formation, as to transform a given volume of liquid to coral graphite one needs only one nucleation event, whereas multiple nucleation events are needed for nodular graphite. Further, no impurity atoms were detected at the nodule centers when examined in the SEM using nondispersive X-ray analysis. Consequently, it was proposed that the nucleating agent involves a carbide (e.g., Cr_{23}C_6 , Co_2C , CaC_2 , Mn_3C) which forms at high temperatures, but upon cooling becomes thermodynamically less stable, thereby

causing precipitation of nascent graphite on its surface which acts as the nucleating agent.⁵³

The room temperature graphite spheroid is the product of at least three processes: (i) nucleation and growth in the liquid; (ii) growth during the eutectic transformation via carbon diffusion through the austenite shell; (iii) growth during cooling to room temperature as the solubility of carbon in austenite decreases. Significant differences in graphite microstructure are found when the experimental

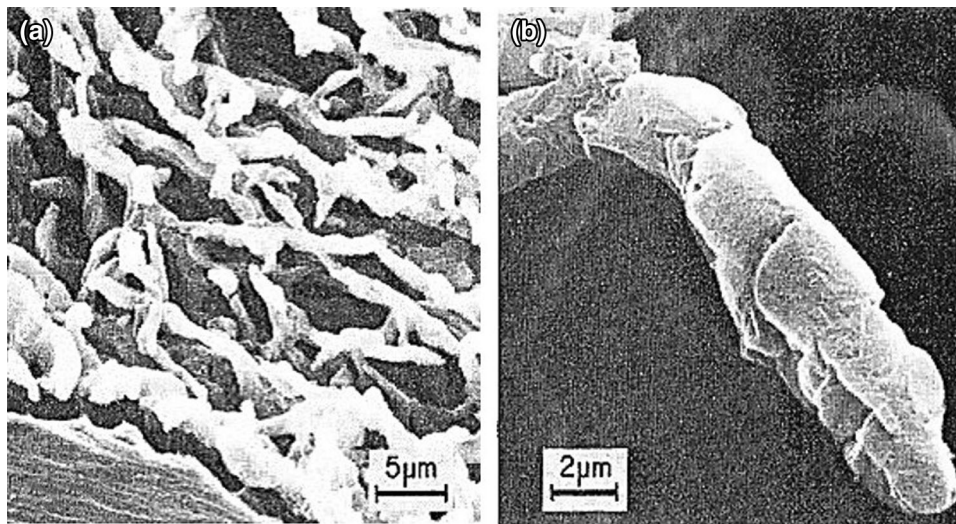


Figure 35. SEM images of coral graphite at two magnifications.⁵²



Figure 36. Deep-etched transition zone in fast-cooled high-purity Fe-C-Si alloy.⁵³

sample is obtained through interrupted solidification versus from the as-cast sample. As seen in Figure 37a from the early work of Lalich and Hitchings,⁵⁴ when solidification is interrupted early, two stages of graphite development can be distinguished: (i) growth of graphite from the liquid around the heterogeneous nucleus and (ii) growth of graphite in contact with the liquid. The graphite around the nucleus appears to grow as curved plates around the spherical (MgCa)S nucleus. In a sample obtained immediately after the end of solidification (Figure 37b), two stages are still observed, with columnar sectors in stage II. Sometimes, the graphite nodule may exhibit the nucleus and all three stages, as seen in Figure 38.⁵⁵ After cooling to room temperature, while the nucleus is visible, the graphite structure is relatively uniform throughout, exhibiting a dendritic orientation produced, maybe, through a cone-helix growth mechanism (Figure 37c), or a concentric orientation resulting from circumferential growth (Figure 37d).

SEM microstructures from a Ce-treated iron after slow solidification are presented in Figure 39, from the early work of Hamasumi.⁵⁶ The microstructure in Figure 39a suggests a radial growth of sectors made of platelets of various orientations. The less regular graphite in Figure 39b shows conical (or maybe polyhedral) graphite aggregates growing radially, with graphite platelets aligned mostly perpendicular to the radius of the aggregate. Figure 39c and d exhibit graphite with dendritic outgrowth, in which sectors extending in the *c*-direction are visible. Hamasumi concluded that the dendrite is an assembly of columnar crystals of graphite growing from nuclei lying along the principal axis of the dendrite. He further states that both spheroidal and dendritic growth consist of columnar crystals, the difference being that SG grows from one nucleus, while graphite dendrites grow from several nuclei scattered along the principal axis of the dendrite. However, on the dendrite in Figure 39f, from the appearance of the orientation of the (0001) graphite planes, it is possible to infer that this is a true, single crystal, dendrite.

A proliferation of papers using transmission electron microscopy to analyze and interpret the room temperature microstructure of spheroidal graphite has occurred in recent years. The pioneering TEM work of Purdy and Audier⁵⁷ demonstrates that after encapsulation of the graphite spheroid into an austenitic shell, graphite growth continues through solid diffusion of carbon through the austenite to the growth front. The amorphous carbon deposited through diffusion at the graphite/austenite interface crystallizes to produce graphite platelets (Figure 40a). Crystallization of graphite from amorphous carbon has also been observed for spheroids produced through processes unrelated to metal casting, such as heating of amorphous carbon in an electronic beam (Figure 40b).⁵⁸

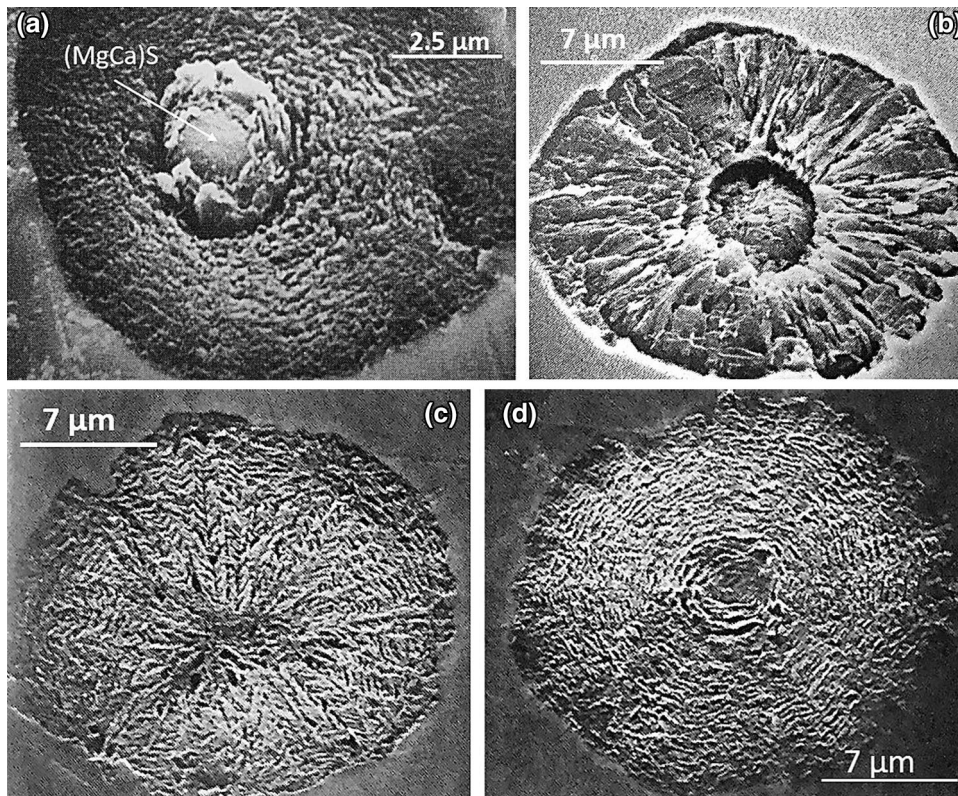


Figure 37. Effect of the growth time (time at which the sample was obtained during solidification and cooling to room temperature) of spheroidal graphite on its microstructure.⁵⁴ (a) quenched from 1288 °C; (b) quenched at the end of the eutectic reaction; (c) as-cast, dendritic orientation; (d) as-cast, concentric orientation

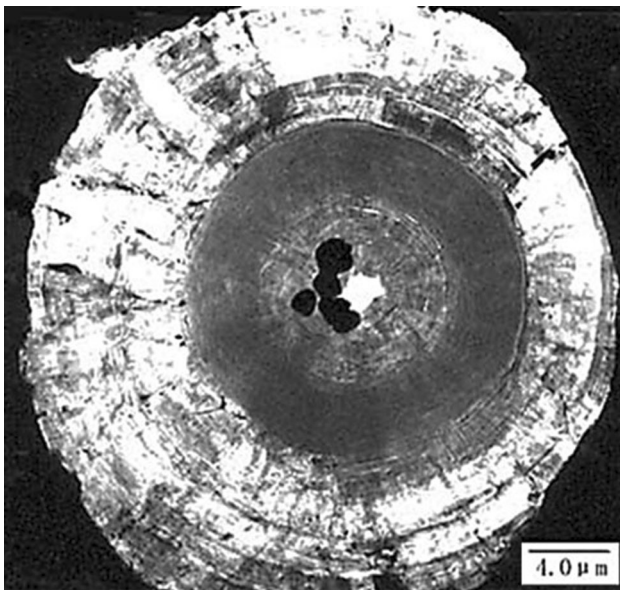


Figure 38. Three-stage growth of a graphite spheroid in an as-cast microstructure; TEM image.⁵⁵

Following a TEM and microdiffraction study, Miao et al.⁴⁵ concluded that the structure of graphite spheroids consists of graphite platelets that have a rhombohedral structure

(Figure 41a) with their [001] directions nearly parallel to the radius of the spheroid. Each platelet is twisted about 2° over a 1 μm length. Randomly orientated graphite, with a hexagonal rather than rhombohedral structure, is located in the interplatelet areas. Based on the crystallographic characterization of the graphite, it is postulated that the growth of SG occurs through the helical growth model proposed by Double and Hellawell.^{36,59} A schematic representation of a cone-helix from a graphite aggregate is proposed in Figure 41b.

TEM work by Hara et al.⁵⁰ summarized in Figure 42 led to the conclusions that the spheroidal graphite has a threefold internal structure, with amorphous central region, annular rings of a layered intermediate region, and an outer region made of large polygonal crystalline platelets in a mosaic-like structure. It appears that no sulfide, oxide or nitride core was necessary for the formation of graphite spheroids.

We note that other TEM work in which the samples were prepared by focused ion beam (FIB) did not report any randomly orientated platelets in the samples.^{60–62} Qing et al.⁶¹ found that graphite shows well-organized lattices with mixture of hexagonal and rhombohedral mixtures.

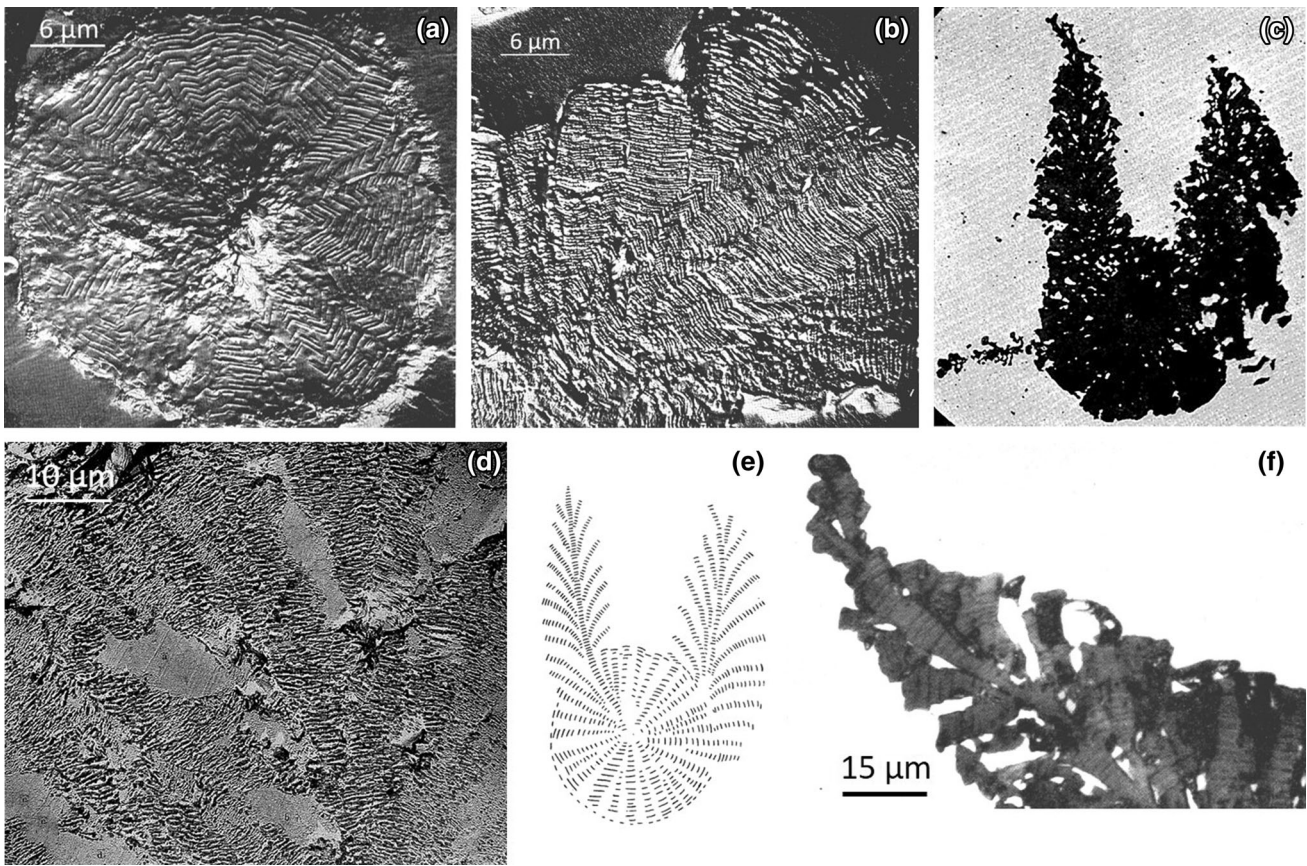


Figure 39. Images of a graphite aggregates obtained from a slow-cooled cerium-treated melt:⁵⁶ (a) graphite spheroid; (b) irregular graphite spheroid; (c) optical micrograph, $\times 250$; (d) magnification of dendritic region in (b); (e) schematic representation of (c); (f) graphite dendrite; cathodic etching

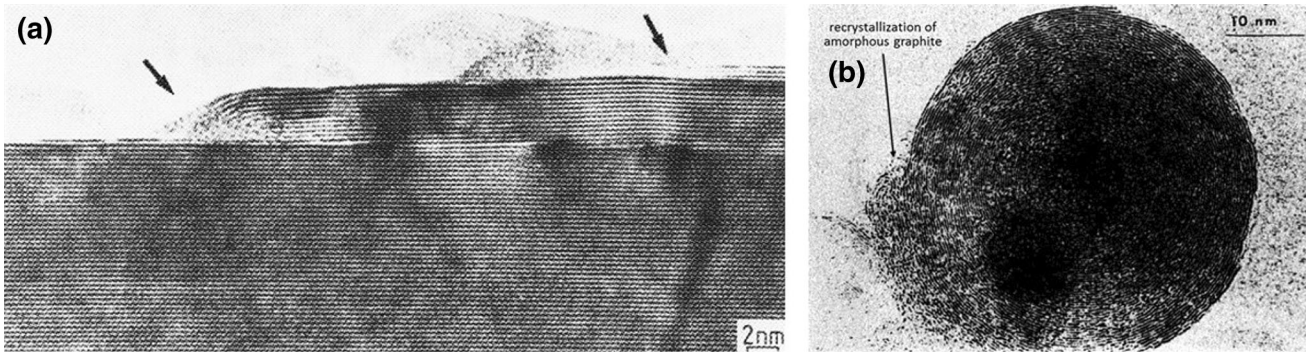


Figure 40. TEM images showing graphite growth through crystallization of amorphous carbon: (a) fractured graphite spheroid showing the growth of graphite platelets (sites indicated by arrows);⁵⁷ (b) graphite spheroid formed by heating amorphous carbon in the electronic beam.⁵⁸

In recent TEM work by Theuwissen et al.⁶² it is argued that flake and spheroidal graphite precipitates consist of blocks stacked upon each other that grow mainly by a 2D nucleation mechanism, as previously suggested by Amini and Abbaschian.⁴ There is a consensus that the room temperature of spheroidal graphite consists of conical sectors made of platelets parallel to one another, as confirmed by numerous TEM studies for cast iron,^{45,50,60–62} graphite in steel,⁴⁴ and pyrolytic graphite spheres.⁶³

Solidification of Degenerate Graphite

Various types of degenerated spheroidal graphite, such as chunky,⁶⁴ dendritic (e.g., Figure 39), exploded or spiky, have been reported in the literature. Spiky graphite, and intergranular (intercellular) form of lamellar graphite, has been found in irons with excessively high Mg residual ($> 0.1\%$),^{65,66} or in irons with high residuals of Pb, Sb or Bi.^{67–69} Rare earths or cerium additions were effective in

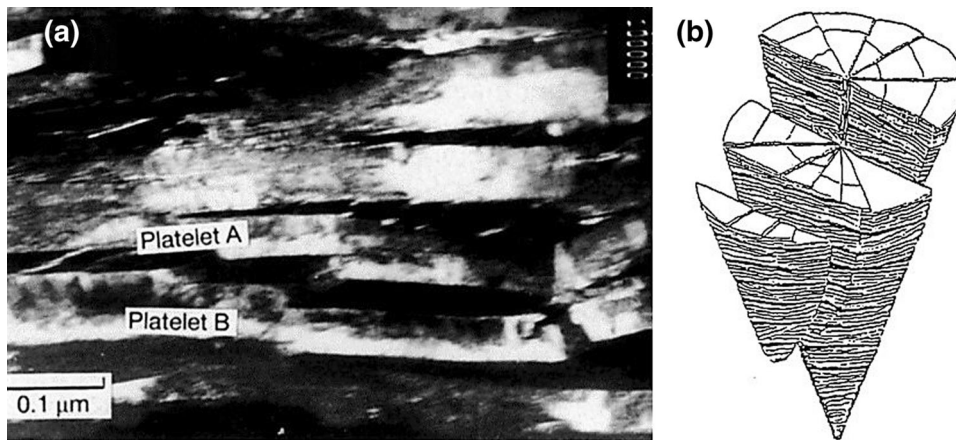


Figure 41. TEM image and proposed mechanism for spheroidal graphite.⁴⁵ (a) bright-field image of platelets from rhombohedral structure of graphite; (b) schematic structure model of a cone from a graphite spheroid

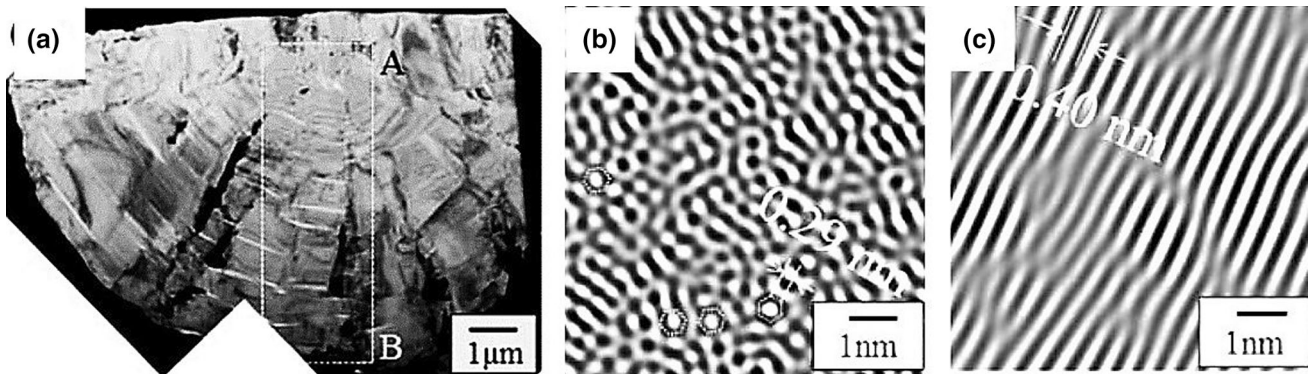


Figure 42. TEM images from a section through a graphite spheroid; (b) and (c) are FFT (fast Fourier transforms) processed TEM images.⁵⁰ (a) section through a graphite spheroid; columnar growth with separation between columns; (b) amorphous central region; (c) crystalline intermediate region

preventing lamellar graphite occurrence, but exceeding amounts of Ce produced chunky and exploded graphite.

Selected SEM micrographs from recent work by Tonn et al.⁷⁰ are presented in Figure 43. Spiky graphite is seen growing out of a spheroidal graphite (Figure 43b). In the work by Basutkar et al.⁶⁶ carbides in high Mg contents iron were annealed. As no spiky graphite formed on the graphite spheroids located in the carbidic areas, it was concluded that spiky graphite must form during solidification of the liquid metal.

The chunky graphite in Figure 43c appears to grow as a dendritic form, different than classic stem dendrites. Graphite platelets and blocks aggregate in the *c*-direction. Note the similarities between the chunky aggregates and the columnar aggregates in the metamorphic graphite in Figure 21.

Critical Analysis of Selected Mechanisms

The complexity of the problem of graphite crystallization and growth in iron melts is illustrated by the large number

of postulated models, periodically reviewed in the literature, e.g., Reference 71–75.

A consensus appears to have been reached in that the building blocks of graphite aggregates are graphite platelets resulting from the stacking of graphene layers. To produce platelets, the graphene sheets must stack/grow in the *c*-direction. These conclusions were reached for nanofibers obtained through catalytic routes (Figure 24), for spheroidal graphite obtained by heat treatment of medium carbon steel (Figure 26b, c), for lamellar graphite in Ni–C alloys,²² and for compacted graphite obtained through interrupted solidification of cast iron (Figure 27a).

Atomically smooth interfaces (faceted crystals such as graphite or silicon) grow parallel to the interface through layer growth. Figure 27a illustrates an example of the thickening of the platelets through growth of additional graphene sheets nucleated at the ledges of the graphite prism in a Fe–C–Si alloy. Amini and Abbaschian⁴ suggested that upon slow cooling of a Ni–3% C supersaturated hypereutectic alloys, the growth of the faceted interfaces of primary graphite is by migration of the ledges produced by

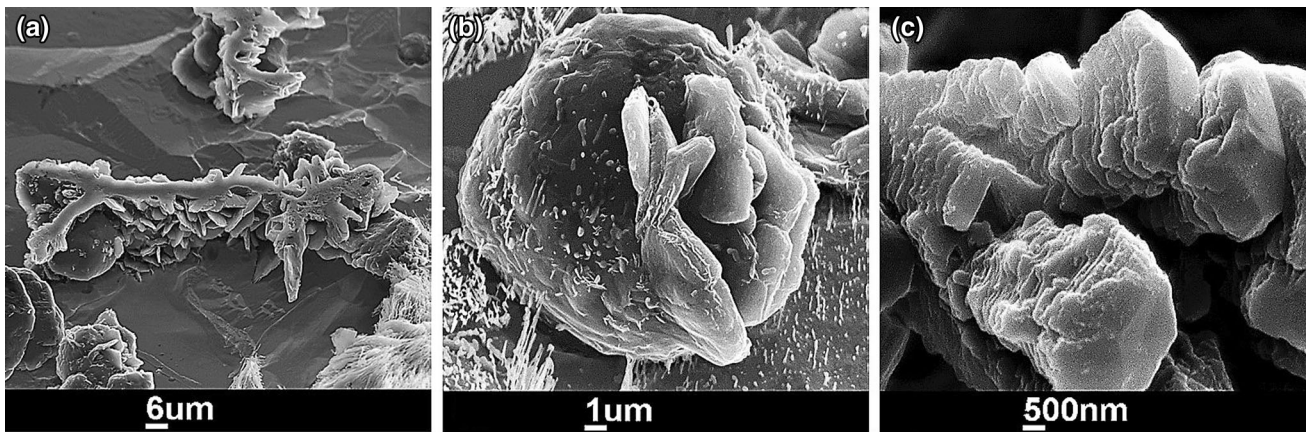


Figure 43. Degenerated spheroidal graphite:⁷⁰ (a) spiky (intergranular) graphite; (b) spiky graphite growing out of a graphite spheroid; (c) chunky graphite

2-D nucleation, resulting in lamellar graphite. This hypothesis was also advocated by other investigators^{60,76} for Fe–C alloys.

Layer growth also occurs in solid state through crystallization of amorphous carbon migrating from the melt through the solid austenite shell, as demonstrated by Purdy and Audier.⁵⁷ Layer growth in solid state was also confirmed for graphite nodules found in 0.38% carbon steel quenched to martensite and then annealed by He et al.⁴⁶ The structure of the 2–5- μm spheroidal nodules suggested radial growth of conical sectors, with an increasing level of orderly arrangement of the graphene layers, beginning from a more disordered arrangement (amorphous) carbon center. The amorphous center was associated with carbon-rich amorphous regions connected with the partially dissolved initial carbide particles that form from the quenched martensite during the early stages of annealing. Layer growth of pyrolytic graphite sphere during a gas–solid transformation was also documented.⁴⁰ In this last case, screw dislocation spiral growth was suggested as the mechanism for layer growth.

While there are many similarities between the growth of ice crystals and that of graphite, there are also significant differences derived from the flexibility of the graphene sheets and the twinning tendency of the graphite platelets. Thus, it is not surprising that the aggregation of platelets to form the various morphologies of graphite found in commercial Fe–C alloys is the subject of much debate. Many mechanisms have been suggested.

One of the most quoted mechanisms is the cone-helix model advanced by Double and Hellawell.^{36,59} It is one of the two mechanisms based on disclinations defect, which are line defects corresponding to “adding” or “subtracting” an angle around a line. When subtracting a wedge from the basic hexagon, the graphene sheet can curl around itself at an angle $\alpha = 60^\circ$ (but not only) to produce a cone (Figure 44a).^{35,37} Extending the cone-helix model to the

solidification of supersaturated Fe–C or Ni–C liquid alloys, Double and Hellawell suggested that if several cone-helices of graphite were simultaneously generated on a nucleus, subsequent growth would fill space in three dimensions by spiral expansion (Figure 44b). This model is also consistent with the observation that the growing ends of whiskers produced through carbon pyrolysis assumed a conical shape.⁷⁷

Cones observed on the surfaces of mm-sized polycrystalline spheroidal metamorphic graphite (Figure 22) were also considered as proof of the operation of the cone-helix mechanism,³⁹ as the texture of the fracture surface of broken cones reveals curved lamellae. Steps on the cone surfaces suggest a layer growth mechanism from a liquid.

An alternative model for the generation of cones is the occurrence of pentagonal defects in the graphene structure, which will result in the bending of the sheet with formation of an apex (Figure 22c). However, the natural cones have a wide distribution of apex angles, which supports a disclination model for cone-helix structures, and suggests that the nucleation of pentagon defects is not the only factor determining graphite cone morphologies.

Yet another alternative mechanism for the formation of pyramids and cones on graphite was postulated by Minkoff.⁷⁸ He suggested that the observed polyhedral faceted surface of a graphite spheroid from a Ni–C alloy is the result of the instability of initial pyramids to form stellar polyhedral forms.

Questions on the operation of the cone-helix model at the scale of a graphite spheroid arise from recent TEM work, e.g., Reference 46, 60, that show that the [0001] direction of graphite planes is parallel to the symmetry axis of the cone in the graphite spheroid. Yet, the cone-helix model generates {0001} graphite planes rotated around the cone symmetry axis that are at an angle with respect to the axis of the cone. This apparent discrepancy can be explained

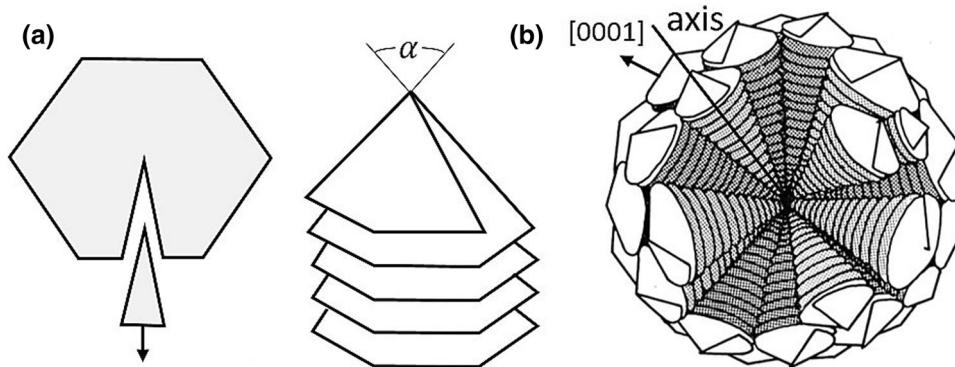


Figure 44. Schematic representation of positive wedge disclination models for growth of graphite aggregates (a) positive wedge disclination and cone-helix growth;³⁷ (b) cone-helix growth of conical sectors.³⁶

through the effect of the sectioning of the TEM sample at different angles (Figure 45). A modified screw dislocation spiral growth mechanism (Figure 46a) was suggested by Miao et al.⁴⁵ as an alternative to the cone-helix mechanism, and used to explain the formation of conical sectors in graphite spheroids produced through annealing of quenched carbon steel.⁴⁶

A second disclination defect, resulting from inserting a wedge from the basic hexagon, is considered to be responsible for helical growth, originally termed “macrospiral” growth by Kvasnitsa et al.³⁵ This mechanism, shown in Figure 46c, is quite different from the cone-helix one. It can produce thick plates that spiral upward during growth, as shown in Figure 18 for metamorphic graphite. In some instances, the product of helical growth is graphite polyhedral blocks. The bending of the graphene sheets induced by disclination could lower the overall symmetry of the aggregate from sixfold to threefold (hypomorphism), which explains the rounding of the platelets. Kvasnitsa et al. further argued that during helical growth, the bending of the sheets will produce increasing lattice strain. At some critical thickness, this elastic energy will become too large, and polygonization would be expected to take place,

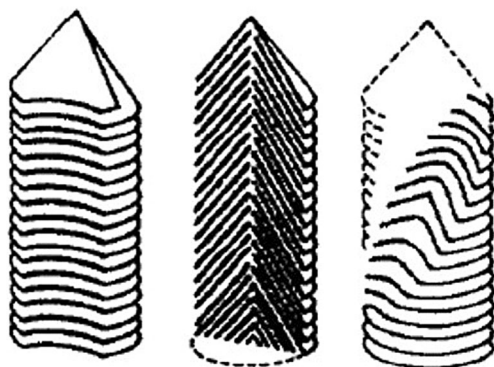


Figure 45. Various sections through a cone-helix showing the arrangement of successive spiral layers;³⁶ note the herring-bone aspect on the right-hand picture

leading to formation of separate crystallites slightly misoriented with respect to each other.

For cast iron, the helical growth mechanism has been illustrated for eutectic crystals of graphite as early as 1975 by Lux et al.²⁴ (Figure 47a), who attributed it to growth inhibition by an impurity particle. The graphite lamellae undergo dendritic branching out of the edges of the lamellae. As seen in Figure 47, the branches curve, climbing in the [0001] direction, and overlap the original graphite plate. If the overlap continues to curve, it can morph into helical growth. Helical growth has also been suggested to operate in the growth of chunky graphite by Liu et al.^{79,80} as shown in the example in Figure 47c.

Positive wedge disclination does not always result in helical growth. If the growing segments do not overlap, hollow prisms may grow, as found in ice crystals and SG in Fe–C–Si alloys (Figure 48).

Sadocha and Gruzlesky²⁵ suggested that graphite spheroids in high-purity Fe–C–Si alloys result from the bending of the graphite platelets, through “circumferential growth,” or “curved crystal growth,” with the principal growth direction along the *c*-axis (Figure 46b). Interrupted solidification experiments on industrial composition Fe–C–Si alloys by Lalic and Hitchings⁵⁴ appear to demonstrate that at the very beginning, the spherical form of the graphite is the result of curved-circumferential crystal growth. As seen in Figure 37, the graphite around the nucleus appears to grow as curved-circumferential plates around the spherical (MgCa)S nucleus. In stage II, concentric or columnar growth occurred. Curved-circumferential growth in early solidification of graphite was also documented in early solidification of hypereutectic Ni–C alloys (Figure 11a).

The morphology of the dendrites in Figures 29a and 33 requires a different mechanism than the classic stem dendrites mechanism. Saratovkin²¹ described the growth of foliated crystals and dendrites as assemblies of thin plates

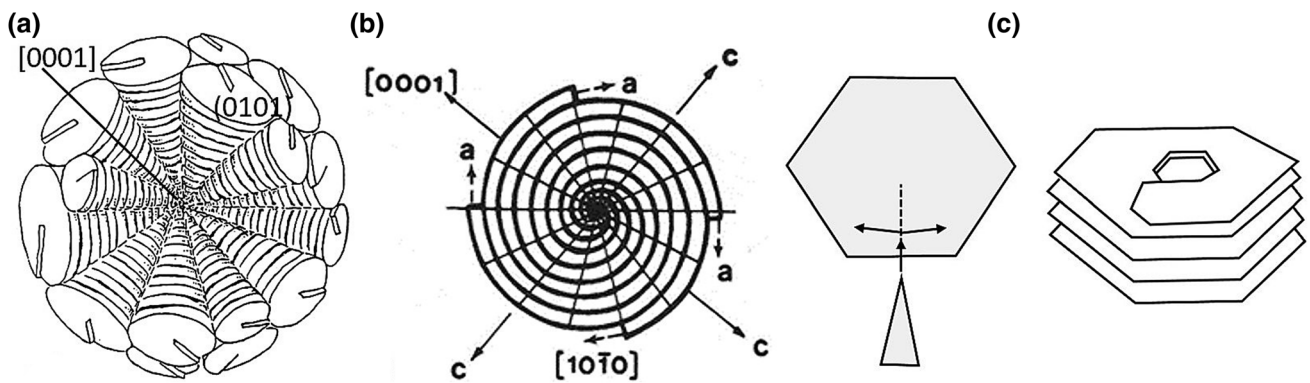


Figure 46. Schematic representation of selected postulated growth mechanisms of graphite aggregates: (a) spiral-dislocation growth of conical sectors;⁴⁵ (b) curved-circumferential growth;²⁵ (c) negative wedge disclination and helical (macro-spiral) growth; from Reference 7 modified after Reference 35

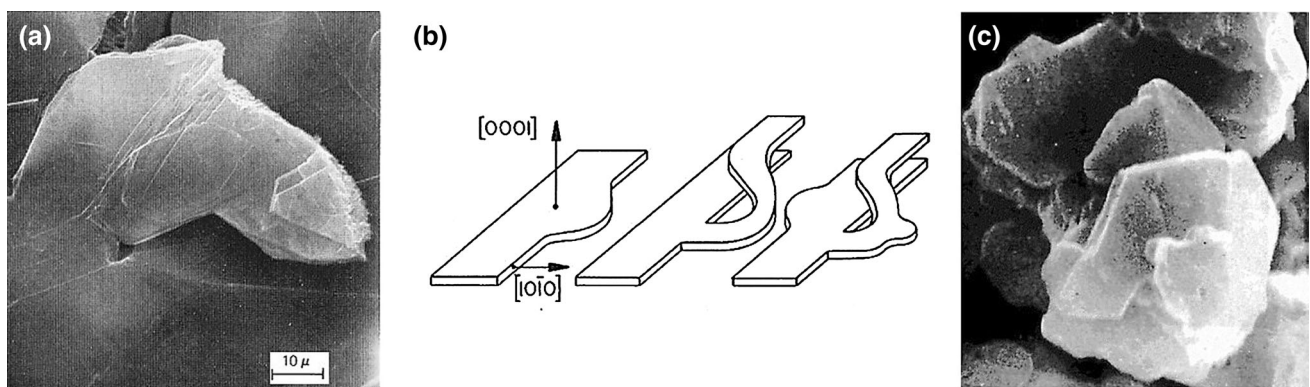


Figure 47. SEM images illustrating helical growth in graphite in Fe-C-Si alloys: (a) lamellar graphite,²⁴ (b) schematic description of dendritic branching in flake graphite normal to the c-axis,²⁴ (c) chunky graphite.⁸⁰

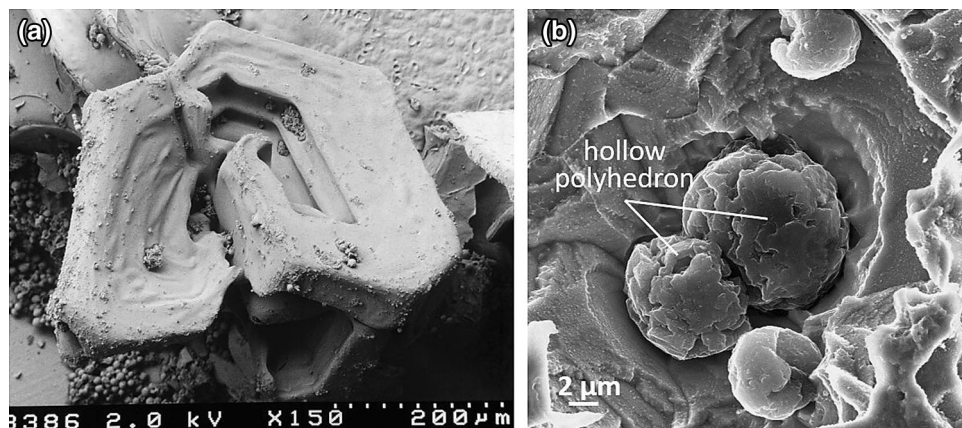


Figure 48. Hollow prisms in ice and graphite: (a) hollow prism (scroll) ice crystal (compliments of Beltsville Agricultural Research Center); (b) hollow polyhedrons in graphite spheroids from a room-temperature sample (compliments of A. Udriou).⁵

separated by solvent impurity layers and suggested that this mechanism operates in the case of graphite in iron alloys. The foliated dendrite growth mechanism for graphite was supported through extensive experimental work by Roviglione and Hermida.⁸¹ In recent research, the authors of this paper argued that the foliated dendrites can grow in a tiled-roof configuration described schematically in

Figure 49a. At higher constitutional undercooling (higher Mg content), the platelets increasingly stack in the [0001] direction and may produce dendritic aggregates (Figure 49b). At sufficiently high undercooling and/or supersaturation, the stacking is predominantly in the [0001] direction, generating columns (Figure 49c).

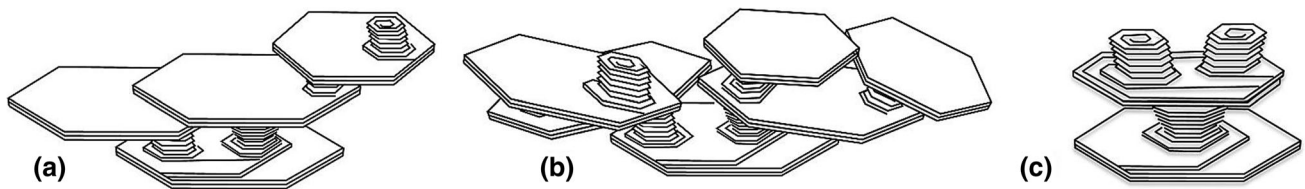


Figure 49. Schematic representation of foliated crystal growth: (a) tiled-roof arrangement; (b) foliated dendrites; (c) columnar foliated crystals.^{5,48}

The initial growth stages in lamellar graphite consists of hexagonal platelets that appear to be foliated dendrites (Figure 29a). In later stages, the graphite is made of layered faceted crystals with a tiled-roof configuration (Figure 30a, c, d). Recent TEM work by Hara et al.⁵⁰ also concluded that the internal structure of flake graphite consisted of thin layers of graphite crystalline platelets arranged in a “mosaic-like” structure, which is the tiled-roof configuration.

The dendritic growth pattern found in an antimony alloyed CG iron (Figure 33) is similar to the dendritic growth of degenerated graphite in Figure 50, in that they both appear to be a combination between stem- and foliated dendrite growth. Polyhedral clusters oriented at various angles with respect to one another are the result of the stacking of the graphite platelets predominantly along the *c*-axis, producing graphite blocks.

The SEM image in Figure 29a confirms that the morphology of compacted graphite includes graphite plates that branch, bend, and stack in the [0001] direction, resulting in columnar blocks and curved segments. TEM work also established that poor nodularity graphite is an aggregation of particles with a complex structure, consisting of large polygonal crystals arranged in a mosaic-like structure.⁵⁰

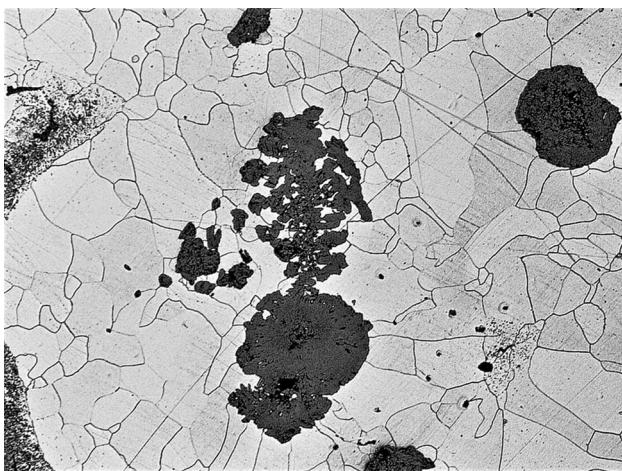


Figure 50. Dendritic outgrowth on a graphite spheroid in a large casting; optical micrograph (compliments A. Udriou).⁵

Foliated dendrite growth was also observed in other analogous systems such as Ni–C and Al-based alloys. The curved plate at the bottom of the graphite spheroid in Figure 11b appears separated from the platelets under it and thus cannot be the result of layer growth. It may be construed as curved foliated dendritic growth. Tiled-roof structure of silicon was observed in eutectic non-modified sand-cast Al9Si3Cu alloy (Figure 9) and that of Al₃Ti plates in an Al–Ti alloy (Figure 17c). Of particular interest are the platelets in Figure 9b, which exhibit the thin connection between plates typical of foliated crystals.

Finally, we must consider the mechanism involved in the growth of columnar, conical, or pyramidal columns that have been observed in ice crystals (Figure 16c), Al–Si alloys (Figure 4a), metamorphic graphite (Figure 21), Ni–C alloys (Figure 11c), and in Fe–C–Si alloys (Figure 37c, 39a, b, c). The differences between the structures of columns found in different systems suggest that more than a single growth mechanism is involved. The pyramidal development of Al–Si and ice crystals can be explained through layer growth. However, for metamorphic graphite, as the platelets of the column present clear separations, they are more probable result of foliated crystal stacking through the mechanism proposed in Figure 49c. An alternative explanation is early helical growth of (0001) layers, with subsequent growth of polyhedral blocks through spiral dislocation or helical growth.³⁵ The growth of small polyhedral blocks on larger hexagonal structure is illustrated in Figure 20b and is also seen on ice crystals in Figure 16a. Thicker polygonized blocks of crystals show a deviation from parallelism of the (0001) planes. Polyhedral growth and the deviation of parallelism of the crystallite blocks may result in nearly spherical aggregates.

Growth in the *c*-direction can also be explained through the twist-tilt boundary mechanism suggested by Frank,³⁸ as discussed earlier in this paper. Some evidence for this growth mechanism can be seen from the arrangement of steps on the pinacoid surfaces in Figure 21. Also note the similarity between the column in the metamorphic graphite in Figure 21 to that of the columnar graphite in the dendritic compacted graphite in Figure 33c.

In Fe–C–Si alloys cooled to room temperature (as-cast), both concentric platelets orientation (Figure 37a) and herring-bone orientation is found (Figure 37c). The microstructure of the exploded spheroid in Figure 39b

exhibits both columnar and inverse conical growth, with concentric and some herring-bone orientation of the platelets. It appears that, if given room for growth, the cylindrical columns develop into conical ones.

Concluding Remarks: Multi-mechanisms Growth of Graphite in Cast Iron

The analysis of the growth of hexagonal and diamond cubic faceted crystals, and of graphite produced through several processes in different alloys presented this paper, demonstrates that crystallization of graphite aggregates evolves through several mechanisms. Crystallization of graphite from iron-carbon melts begins with that of hexagonal faceted *graphite platelets*, which are the basic building blocks of the graphite aggregates. They thicken through layer growth from the edges of the platelet, through 2-D nucleation or spiral dislocation growth, and then aggregate by various mechanisms to produce the known graphite shapes in cast iron.

At low constitutional undercooling (supersaturation) and low cooling rate, graphite grows in the general *a*-direction as large plates made of hexagonal faceted platelets, distributed in a *tiled-roof configuration*. Clear evidence of *foliated dendrite* growth was found in low-sulfur LG iron, in hypoeutectic LG melts with 0.18%Ti, and in chunky graphite.⁷ This is also supported by micrographs in other recent research,^{48,82} and is consistent with the schematic model proposed previously (Figure 51a). The platelets twin^{48,83} and branch as they grow. This mechanism was found to be operational for foliated Al₃Ti crystals in Al-Ti alloys³⁴ and foliated silicon crystals in Al-Si.²⁰

Local conditions may be conducive to *dendritic growth of graphite*. Yet, unlike the common stem dendrites found in ice and silicon crystals, the graphite dendrites are platelets stacked in the [0001] direction, as represented schematically in Figure 51c. The stacking may occur through

foliated growth or through *layer growth*. While these mechanisms are also active during growth of chunky graphite, published micrographs^{7,70} strongly support an additional mechanism, the *helical growth* mechanism (not to be confused with the cone-helix mechanism of Double and Hellawell). Helical growth was documented for both LG and SG graphite, and for metamorphic graphite.

Additions of compacting elements such as Mg or Ce to the melt, or higher cooling rate, increase the local supersaturation. The direction of the [0001] axis of the platelets changes continuously during growth, and the graphite plates increasingly curve producing “curly graphite” (Figure 51b, 52a). While still growing predominantly along the *a*-axis, the platelets begin stacking along the *c*-axis. The lamellar habitat is gradually lost. Further increase in supersaturation and/or undercooling results in crystallization of tadpole and compacted graphite. The platelets appear to hold constant direction of the *c*-axis, but the graphite aggregate curves by continuously changing the *a*-direction, a mechanism summarized in Figure 52b. The platelets of the tadpole outgrowth in Figure 52b appear to have a different orientation than the concentric platelets surrounding the nucleus that are probably the result of *curved circumferential growth*. Additional increase in supersaturation produces graphite spheroids that grow through curved circumferential growth in the initial stages (stage I), as shown schematically in Figure 51d, a mechanism consistent with findings in quenching experiments for both Fe-C^{7,54} and Ni-C^{4,84} alloys. However, as in some instances the curved platelets are not in direct contact along the (0001) planes (e.g., the outermost platelets in Figure 11b are separated from the platelets under them), a combined curved-circumferential and foliated dendrite growth may be suggested.

TEM work found amorphous (or low crystalline) central regions in graphite spheroids that did not have a sulfide, oxide or nitride core⁵⁰ and in the center of graphite spheroids in steel.⁴⁴ If extensive curved-circumferential-

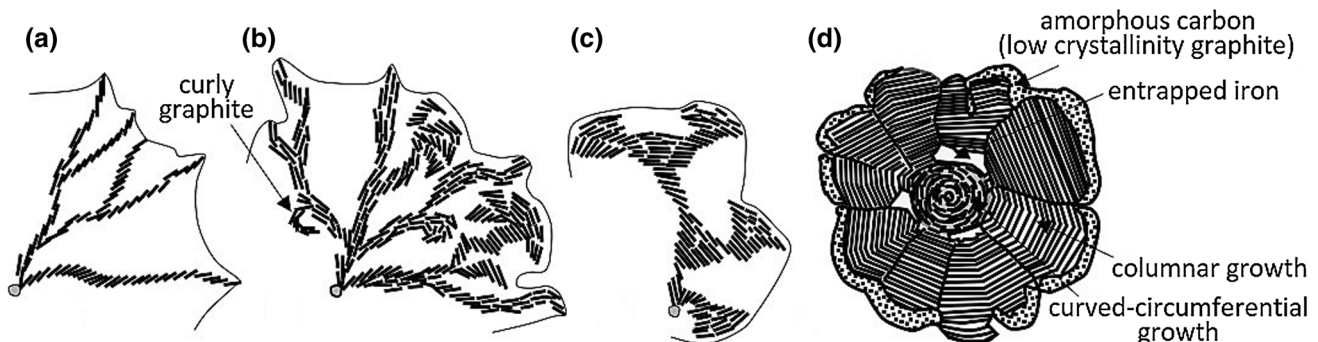


Figure 51. Schematic model illustrating the role of graphite platelets in the construction of various graphite aggregates: (a) tiled-roof lamellar graphite;⁴⁸ (b) curly, lamellar and compacted graphite;⁴⁸ (c) chunky and degenerated spheroidal graphite;⁴⁸ (d) spheroidal graphite

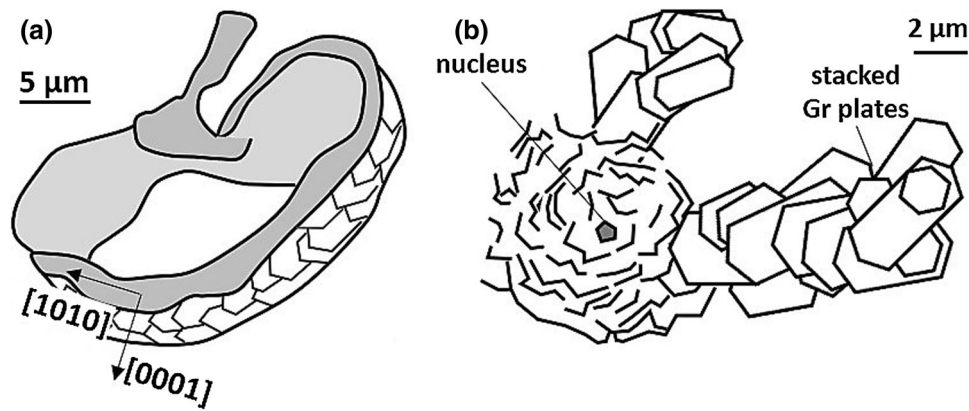


Figure 52. Schematic representation of two different curving mechanisms: (a) curved growth of curly graphite—the direction of the $[1010]$ a -axis and of the $[0001]$ c -axis of the platelets changes continuously; (b) outcrops of a tadpole graphite—the c -axis of the platelets remains constant, but the direction of the a -axis changes

foliated growth occurs in stage I, the central region of the spheroidal may exhibit a low degree of crystallization. The highly ordered core of spheroids found in some other research^{61,62} may be the result of recrystallization during cooling or of solidification through the helical mechanism that produces thick graphite plates.

Radiography using a synchrotron radiation X-ray source found that early solidification of SG from the liquid can also proceed with columnar conical sectors.⁸⁵

Subsequent development after encapsulation of graphite by austenite (stage II) includes further stacking of the graphite platelets into clusters of polyhedral blocks with further polygonization and hypomorphism, and highly curved graphite aggregates. The end result of crystallization of spheroidal graphite are conical sectors made of platelets parallel to one another (Figure 51d), similar to the pyramidal sectors found in ice and silicon crystals, as confirmed by numerous TEM studies for cast iron,^{45,50,61,62} graphite in steel,⁴⁴ and pyrolytic graphite spheres.⁴⁰ As to the mechanism through which they arrived at this arrangement, several options are available, including layer growth, foliated crystal stacking, and helical growth. The *cone-helix mechanism* could be responsible for the hearing-bone appearance of graphite platelets in some spheroids.

The graphite platelets may also grow through crystallization of amorphous carbon diffusing from the liquid. TEM evidence of such growth has been documented for both spheroidal graphite in a Fe–C alloy,⁵⁷ and for spheroids produced through processes unrelated to metal casting, such as heating of amorphous carbon in an electronic beam.⁵⁸ Crystallization of the amorphous carbon can occur at all stages of solidification. It may thicken the existing platelets or grow new platelets. It is clearly seen in examples of stage III SG growth (Figure 3) and represented schematically in Figure 51d.

During cooling after solidification, carbon solubility in the austenite decreases and diffuses to the graphite. This is stage III of graphite growth occurring in the solid matrix. Because of the high carbon diffusion rates associated with the elevated temperature, recrystallization of graphite may result in the morphing of stage III carbon into the conical sector structure of stage II. However, because carbon is also deposited at relatively low temperatures during austenite cooling, or eutectoid transformation, stage III of graphite growth may produce less organized graphite, or even amorphous carbon at the periphery of the graphite spheroid.

While a good understanding of the diverse mechanisms responsible for the formation of the large variety of graphite shapes found in industrial cast iron has been achieved (the *how?*), there is still a lot to be learned about the reasons for all these mechanisms (the *why?*). The discussion should start with the curved growth of graphite. The two main reasons suggested for curved growth of graphite are surface energy and impurity level (see extensive literature review in Reference 74).

It is difficult to accept that *surface energy* acts as a compacting force on the overall graphite crystal. Indeed, if a crystal becomes larger than 1 μm, the change in free energy because of departure from equilibrium becomes small compared with the supersaturation necessary for crystal growth.⁸⁶ It follows that capillary forces will not shape the overall graphite crystal in the aftermath of nucleation. However, surface energy effects at the level of the crystal lattice scale do have a role, as in low oxygen iron–magnesium alloys, the interface energy of the liquid/prism face of graphite is higher than that of the liquid/basal face of graphite. This led McSwain and Bates⁸⁷ to conclude that graphite grows from the melt normal to the plane with the lowest interfacial energy, which is the c -direction for the Fe–C–Mg alloy and the a -direction for the Fe–C–S

alloy used in their experiments. The curved circumferential growth appears to be produced by changes in surface energy.

The theories based on the *impurity level* argue that the final graphite shape is the outcome between the interaction of the reactive compacting element (Mg, Ce, etc.) and the surface-active anti-compacting elements (O and S). Indeed, the lamellar-to-compacted-to-spheroidal graphite transition is favored by decreasing amounts of anti-compacting impurities and increasing amounts of compacting impurities. It is also known that the undercooling is affected by elements that absorb on the graphite/iron interface and by the fault density induced by impurity elements.

The role of impurities on interface mobility and thus on the mechanism of crystal growth must also be considered. There are two main mechanisms for the movement of the solid/liquid interface to be considered, continuous and lateral growth. *Continuous growth*, controlled by solute transport to the interface, is typical for atomically rough non-faceted interfaces, such as iron or silicon. It requires small driving forces and thus small undercooling. *Lateral growth* requires larger driving forces, and thus larger undercooling, and is typical for atomically smooth faceted crystals such as graphite. Two mechanisms are known for lateral growth, 2-D nucleation of a new layer, and defect controlled growth, such as screw dislocation nucleation. The latter requires significantly lower driving force. Experiments on iron melts confirmed that the removal of surface-active elements (S, O) promotes the faceting of the graphite prism face, which decreases mobility.⁸⁸ This explains the higher undercooling in industrial melts where S and O have been decreased through additions of Mg or Ce. However, computer modeling of the dynamics of crystal growth by Gilmer concluded that an impurity that forms strong bonds with the host species sticks to the crystal surface and promote nucleation, generating a growth velocity comparable to that of defect controlled growth.⁸⁹ This appears to support the 2-D nucleation theory of Amini and Abbaschian.⁴

Scanning Auger microprobe studies^{90–92} found that sulfur and oxygen were adsorbed at the lamellar graphite/metal interfaces in some two or three atomic layers, while the spheroidal graphite/metal and the graphite were free of these elements. For both compacting elements modification and vacuum casting, it is suggested that it is the absence of sulfur and oxygen at the graphite/metal interface that produces spheroidal graphite. In Mg-modified iron, neither Mg, nor O or S, were detected on the graphite surface, but appeared combined as Mg–S–P inclusions.⁹⁰ This seems to imply that Mg does not act directly on the graphite, but rather that it is a scavenger of the impurities that stabilize lamellar graphite. However, as good spheroidal graphite cannot be obtained by simply reducing the S and O content to zero, and as Mg-containing irons produce good graphite

spheroids, while Ce or Ca-containing irons only produce quasi-spheroidal graphite, it is reasonable to conclude that the reactive impurities also play a direct role in the growth of graphene.

Based on simulations with a molecule editor program, Muhmond and Fredriksson⁹³ concluded that in the absence of defects, flexible graphene sheets grow mainly in the *a*-direction. Growth along the *c*-direction, and thus conical sectors or spheroidal growth of graphite, is favored by pentagonal rings generated by impurity elements (O, N), vacancies, and carbon ring defects, as they induce curvature in the basal plane. Other elements (S, Se, B) attach to the basal plane and stabilize lamellar growth.

From the preceding discussion, it follows that impurities have at least a dual role in graphite crystallization in Fe–C alloys, through their direct effect on the graphene sheets: (i) they affect nucleation of new layers on the graphene sheet and thus graphene thickening in the [0001] direction and (ii) they may induce curvature in the (0001) planes, resulting in the bending of the graphene sheets.⁷ This further emphasizes the need for better understanding of the influence of impurities.

The substrate on which the graphene growth (the nucleus) directly affects the morphology of the final aggregate. Experimental evidence is available on the growth of graphite spheroids obtained through solid/gas transformations (carbon nano-fibers, e.g., Reference 42) or through solid/solid transformations (graphite spheroids in steel, e.g., Reference 40).

REFERENCES

1. A.K. Geim, K.S. Novoselov, The rise of graphene. *Nat. Mater.* **6**, 183–191 (2007)
2. E. Fraś, M. Górný, H. Lopez, *Metall. Mater. Trans. A* **38A**, 385–395 (2007)
3. D.K. Bandyopadhyay, D.M. Stefanescu, I. Minkoff, S.K. Biswal, in *Physical Metallurgy of Cast Iron IV*, ed. by G. Ohira, T. Kusakawa, E. Niyama, Tokyo, Mat. Res. Soc. Proc., Pittsburgh, PA, 1989, p. 27
4. S. Amini, R. Abbaschian, Nucleation and growth kinetics of graphene layers from a molten phase. *Carbon* **51**, 110–123 (2013)
5. D.M. Stefanescu, G. Alonso, P. Larrañaga, E. De la Fuente, R. Suarez, On the crystallization of graphite from liquid iron–carbon–silicon melts. *Acta Mater.* **107**, 102–126 (2016)
6. S.E. Franklin, R.A. Stark, Further use of secondary ion mass spectroscopy in the study of graphite morphology control in cast iron, in *The Physical Metallurgy of Cast Iron*, ed. by H. Fredriksson and M. Hillert, Stockholm,

- Mat. Res. Soc. Symposia Proc., North-Holland, NY, 1985, pp. 25–35
7. D.M. Stefanescu, G. Alonso, P. Larrañaga, E. De la Fuente, R. Suarez, Reexamination of crystal growth theory of graphite in iron-carbon alloys. *Acta Mater.* **139**, 109–121 (2017)
 8. W.C. O'Mara, *Handbook of Semiconductor Silicon Technology*. (William Andrew Inc., ISBN 0-8155-1237-6, 1990), pp. 349–352
 9. A. Hellawell, The of growth and structure of eutectics with silicon and germanium. *Prog. Mater. Sci.* **15**, 3–78 (1970)
 10. C.R. Loper, C.B. Kim, K.M. Htun, R.W. Heine, Analogous solidification in cast irons and aluminum–silicon alloys, in *Recent Research on Cast Iron*, ed. by H.D. Merchant (Gordon and Breach, New York, 1968), pp. 363–387
 11. D.A. Granger, R. Elliott, Aluminum–silicon alloys, in *ASM Handbook*, vol. 15, Casting, ed. by D.M. Stefanescu (ASM International, Novelty, 1988), pp. 159–168
 12. V.L. Davies, J.M. West, Factors affecting modification of aluminium-silicon eutectic. *J. Inst. Met.* **92**, 175 (1963–64)
 13. M.G. Day, Primary silicon spherulites in aluminium–silicon alloys. *Nature* **219**, 1357–1358 (1968)
 14. B. Lux, F. Mollard, I. Minkoff, On the formation of envelopes around graphite in cast iron, in *The Metallurgy of Cast Iron*, ed. by B. Lux, I. Minkoff, F. Mollard (Georgi Publishing Co., St Saphorin, 1974), pp. 371–401
 15. H. Nakae, H. Shin, Similarity in solidification mode between Fe–C and Al–Si alloys. *Int. J. Cast Met. Res.* **11**(5), 345–349 (1999)
 16. H. Fredriksson, M. Hillert, N. Lange, The modification of aluminum–silicon alloys by sodium. *J. Inst. Met.* **101**, 285–299 (1973)
 17. H. Fredriksson, U. Åkerlind, *Solidification and Crystallization Processing in Metals and Alloys* (Wiley, London, 2012), p. 486
 18. Y.T. Pei, J.Th.M. De Hosson, Producing functionally graded coatings by laser-powder cladding, *JOM-e*, **52**(1) (2000).
www.tms.org/pubs/journals/JOM/0001/Pei/Pei-0001.html
 19. K. Fujiwara, K. Maeda, N. Usami, K. Nakajima, Growth mechanism of si-faceted dendrites. *Phys. Rev. Lett.* **101**, 055503 (2008)
 20. E. Tillová, M. Chalupová, L. Hurtalová, Evolution of phases in a recycled Al–Si cast alloy during solution treatment, in *Scanning Electron Microscopy*, ed. by V. Kazmiruk (InTech, Chapters published March 09, 2012). <https://doi.org/10.5772/34542>
 21. D.D. Saratovkin, *Dendritic Crystallization* (Consultants Bureau, New York, 1959)
 22. D.D. Double, A. Hellawell, The structure of flake graphite in Ni–C eutectic alloy. *Acta Metall.* **17**, 1071–1083 (1969)
 23. I. Minkoff, I. Einbinder, Official Exchange Paper—Israel, International Foundry Congress (1963) pp. 139–143
 24. B. Lux, I. Minkoff, F. Mollard, E. Thury, Branching of graphite crystals growing from metallic solution, in *The Metallurgy of Cast Iron*, ed. by B. Lux, I. Minkoff, F. Mollard (Georgi Publishing Co., St Saphorin, 1975), pp. 495–508
 25. J.P. Sadocha, J.E. Gruzleski, The mechanism of graphite spheroid formation in pure Fe–C–Si alloys, in *The Metallurgy of Cast Iron*, ed. by B. Lux, I. Minkoff, F. Mollard (Georgi Publishing Co., St Saphorin, 1975), pp. 443–459
 26. V.F. Petrenko, R.W. Whitworth, *Physics of Ice* (Oxford University Press, ISBN 9780198518945, 1999)
 27. R. Hooke, *Micrographia* (Council of the Royal Society, 1664)
 28. <http://www.snowcrystals.com/science/science.html>
 29. U. Nakaya, *Snow Crystals: Natural and Artificial* (Cambridge University Press, Cambridge, 1954)
 30. B.J. Mason, Ice, in *The Art and Science of Growing Crystals*, ed. by J.J. Gilman (Wiley, New York, 1963)
 31. C. Magono, C.W. Lee, Meteorological classification of natural snow crystals. *J. Fac. Sci. Hokkaido Univ. Jpn. Ser. VII II*(4), 321–335 (1966)
 32. K.G. Libbrecht, <http://www.snowcrystals.com>
 33. J.W. Barrett, H. Garcke, R. Nürnberg, Numerical computations of faceted pattern formation in snow crystal growth. *Phys. Rev. E* **86**, 011604 (2012)
 34. D.H. St, L.M. Hogan John, Metallography and growth crystallography of Al₃Ti in Al–Ti alloys up to 5 wt% Ti. *J. Cryst. Growth* **46**, 387–398 (1979)
 35. V.N. Kvasnitsa, V.G. Yatsenko, J.A. Jaszczak, Disclinations in unusual graphite crystals from anorthosites of Ukraine. *Can. Mineral.* **37**, 951–960 (1999)
 36. D.D. Double, A. Hellawell, Cone-helix growth forms of graphite. *Acta Metall.* **22**, 481–487 (1974).
[https://doi.org/10.1016/0001-6160\(74\)90101-1](https://doi.org/10.1016/0001-6160(74)90101-1)
 37. S. Amelinckx, W. Luyten, T. Krekels, G. Van Tendeloo, J. Van Landuit, Conical, helically wound, graphite whiskers: a limiting member of the “fullerenes”. *J. Cryst. Growth* **121**, 543–558 (1992)
 38. F.C. Frank, The influence of dislocations on crystal growth. *Disc. Faraday Soc.* **5**, 48–54 (1949)
 39. J.A. Jaszczaka, G.W. Robinson, S. Dimovskic, Y. Gogotsic, Naturally occurring graphite cones. *Carbon* **41**, 2085–2092 (2003)
 40. D.D. Li, R.X. Tan, J.X. Gao, B.Q. Wei, Z.Q. Fan, Q.Z. Huang, K.J. He, Comparison of pyrolytic graphite spheres from propylene with spheroidal graphite nodules in steel. *Carbon* **111**, 428–438 (2017)
 41. H. Daniels, R. Brydson, A. Brown, B. Rand, Quantitative valence plasmon mapping in the TEM: viewing physical properties at the nanoscale. *Ultramicroscopy* **96**(3–4), 547–558 (2003).
[https://doi.org/10.1016/s0304-3991\(03\)00115-3](https://doi.org/10.1016/s0304-3991(03)00115-3)

42. S.H. Yoon, S.G. Lim, S.H. Hong, W.M. Qiao, D.D. Whitehurst, I. Mochida, B. An, K. Yokogawa, A conceptual model for the structure of catalytically grown carbon nano-fibers. *Carbon* **43**, 1828–1838 (2005)
43. K. Roesch, Recent developments in the area of malleable cast iron. *Stahl Eisen* **24**, 1747 (1957)
44. K. He, H.R. Daniels, A. Brown, R. Brydson, D.V. Edmonds, An electron microscopic study of spheroidal graphite nodules formed in a medium-carbon steel by annealing. *Acta Mater.* **55**, 2919–2927 (2007)
45. B. Miao, D.O. Northwood, W. Bian, K. Fang, M. Fan, Structure and growth of platelets in graphite spherulites in cast iron. *J. Mater. Sci.* **29**, 255–261 (1994). <https://doi.org/10.1007/BF00356601>
46. K. He, A. Brown, R. Brydson, D. Edmonds, Analytical electron microscope study of the dissolution of the Fe₃C iron carbide phase (cementite) during a graphitisation anneal of carbon steel. *J. Mater. Sci.* **41**(16), 5235–5241 (2006)
47. E.V. Zakhartchenko, E.P. Akimov, C.R. Loper, Kish graphite in gray cast iron. *AFS Trans.* **87**, 471–476 (1979)
48. D.M. Stefanescu, R. Huff, G. Alonso, P. Larrañaga, E. De la Fuente, R. Suarez, On the crystallization of compacted and chunky graphite from liquid multi-component iron–carbon–silicon based melts. *Metall. Mater. Trans.* **47**, 4012–4023 (2016)
49. K.M. Fang, G.C. Wang, X. Wang, L. Huang, G.D. Deng, The microstructure and metamorphic regularity of graphite in cast iron, in *Science and Processing of Cast Iron VIII*, ed. by Y.X. Li, H.F. Shen, Q.G. Xu, Z.Q. Han (Tsinghua Univ. Press, Beijing, 2006), pp. 181–187
50. T. Hara, T. Kitagawa, K. Kuroki, S. Saikawa, K. Terayama, S. Ikeno, K. Matsuda, Morphologies of some graphite in ductile iron. *Mater. Trans. JIMM* **55**(9), 1500–1505 (2014)
51. B. Lux, On the theory of nodular graphite formation in cast iron. *Cast Met. Res. J. March* **8**, 25–28 (1972)
52. B. Lux, Discussion on transition from undercooled to flake graphite, in *The Metallurgy of Cast Iron*, ed. by B. Lux, I. Minkoff, F. Mollard (Georgi Publishing Co., St Saphorin, 1975), pp. 289–292
53. B. Dhindaw, J.D. Verhoeven, Nodular graphite. Formation in vacuum melted high purity Fe–C–Si alloys. *Metall. Trans. A* **11A**, 1049–1057 (1980)
54. M.J. Lalich, J.R. Hitchings, Characterization of inclusions as nuclei for spheroidal graphite in ductile cast iron. *AFS Trans.* **84**, 653–664 (1976)
55. K.M. Fang, *Atlas of the Morphology and Microstructure of the Graphite in Cast Iron* (Science Publ. Co. of China, 2000)
56. M. Hamasumi, A newly observed pattern of imperfect graphite spherulite in nodular iron. *Trans. JIM* **6**, 234–239 (1965)
57. G.R. Purdy, M. Audier, Electron microscopical observations of graphite in cast irons, in *The Physical Metallurgy of Cast Iron*, ed. by H. Fredriksson, M. Hillert Stockholm, Mat. Res. Soc. Symposia Proc., North-Holland, NY, 1985, pp. 13–23
58. D. Ugarte, Curling and closure of graphitic networks under electron-beam irradiation. *Nature* **359**, 707–709 (1992)
59. D.D. Double, A. Hellawell, Growth structure of various forms of graphite, in *The Metallurgy of Cast Iron*, ed. by B. Lux, I. Minkoff, F. Mollard (Georgi Publishing Co., St Saphorin, 1975), pp. 509–528
60. J.P. Monchoux, C. Verdu, G. Thollet, R. Fougères, A. Reynaud, Morphological changes of graphite spheruloids during heat treatment of ductile cast irons. *Acta Mater.* **49**, 4355–4362 (2001)
61. J. Qing, V.L. Richards, D.C. Van Aken, Growth stages and hexagonal-rhombohedral structural arrangements in spheroidal graphite observed in ductile iron. *Carbon* **116**, 456–469 (2017)
62. K. Theuwissen, J. Lacaze, L. Laffont, Structure of graphite precipitates in cast iron. *Carbon* **96**, 1120–11286 (2016)
63. D.D. Li, R.X. Tan, J.X. Gao, B.Q. Wei, Z.Q. Fan, Q.Z. Huang, K.J. He, Comparison of pyrolytic graphite spheres from propylene with spheroidal graphite nodules in steel. *Carbon* **111**, 428–438 (2017)
64. H. Itofuji, H. Uchikawa, *Trans. AFS* **98**, 429–448 (1990)
65. J.F. Ellis, C.K. Donoho, Magnesium content and graphite forms in cast iron. *AFS Trans.* **66**, 203–209 (1958)
66. P.K. Basutkar, C.S. Park, R.E. Miller, C.R. Loper, Formation of spiky graphite in high magnesium ductile iron castings. *AFS Trans.* **81**, 180–184 (1973)
67. E.N. Pan, C.N. Lin, H.S. Chiou, Effects of lead and solidification conditions on graphite structure of heavy-section DI. *AFS Trans.* **103**, 265–273 (1995)
68. R.K. Buhr, The effects of Pb, Sb, Bi and Ce on microstructure of heavy section nodular iron castings. *AFS Trans.* **79**, 247–252 (1971)
69. A. Javaid, C.R. Loper, Production of heavy-section ductile cast iron. *AFS Trans.* **103**, 135–150 (1995)
70. B. Tonn, J. Lacaze, S. Duwe, Degenerated graphite growth in ductile iron, in: *Science and Processing of Cast Iron*, Jönköping, Sweden, 2017
71. I. Minkoff, *The Physical Metallurgy of Cast Iron* (Wiley, New York, 1983)
72. R. Elliott, *Eutectic Solidification Processing* (Butterworth, London, 1983)
73. D.M. Stefanescu, Cast Iron, in *ASM Handbook*, vol. 15, Casting, ed. by D.M. Stefanescu (ASM International, Metals Park, 1988), pp. 168–181
74. C.A. van den Velde, A new approach to the solidification of ductile iron, in *The Ductile Iron Society's 1998 Keith D. Millis World Symposium on Ductile Iron*, Hilton Head, S. Carolina 1998, pp. 143–187

75. D.M. Stefanescu, *Science and Engineering of Casting Solidification*, 3rd edn. (Springer, Berlin, 2015), pp. 454–479
76. J. Lacaze, J. Bourdie, M.J. Castro-Roman, A 2-D nucleation-growth model of spheroidal graphite. *Acta Mater.* **34**, 230–235 (2017)
77. M.B. Haanstra, W.F. Knippenber, G. Verspui, in *Proceedings of the 5th European Congress on Electron Microscopy*, Manchester, Institute of Physics, 1972, p. 214
78. I. Minkoff, The spherulitic growth in graphite, in *The Physical Metallurgy of Cast Iron*, ed. by H. Fredriksson, M. Hillert, Stockholm, Mat. Res. Soc. Symposia Proc., North-Holland, NY, 1985, pp. 37–45
79. P.C. Liu, C.R. Loper, T. Kimura, H.K. Park, Observations on the graphite morphology in cast iron. *AFS Trans.* **88**, 97–118 (1980)
80. P.C. Liu, C.L. Li, D.H. Wu, C.R. Loper, SEM study of chunky graphite in heavy section ductile iron. *AFS Trans.* **91**, 119–126 (1983)
81. A.N. Roviglione, J.D. Hermida, From flake to nodular: a new theory of morphological modification in gray cast iron. *Metall. Mater. Trans.* **35B**, 313–330 (2004)
82. W.L. Guesser, C.S. Cabezas, L.C. Guedes, A.M. Zanatta, High temperature strength of cast irons for cylinder heads, in *Science and Processing of Cast Iron*, Jönköping, Sweden, 2017
83. E. Moumeni, N.S. Tiedje, A. Horsewell, J.H. Hattel, A TEM Study on the Microstructure of Fine Flaky Graphite, in *52nd International Foundry Conference*, Portoroz, Slovenia, 2012
84. J. Qing, V.L. Richards, D.C. Van Aken, Examination of austenite solidification and spheroidal graphite growth in Ni–Fe–C alloys, in *Advances in the Science and Engineering of Casting Solidification*, ed. by L. Nastac et al. (TMS, Wiley, Hoboken, New Jersey, 2015), pp. 277–285
85. K. Yamane, H. Yasuda, A. Sugiyama, T. Nagira, M. Yoshiya, K. Morishita, K. Uesugi, A. Takeuchi, Y. Suzuki, Influence of Mg on solidification of hypereutectic cast iron: x-ray radiography study. *Metall. Mater. Trans. A* **46A**, 4937–4946 (2015)
86. F.C. Frank, in *Growth and Perfection of Crystals*, ed. by R.H. Doremus, B.W. Roberts, D. Turnbull (Wiley, New York, 1958)
87. R.H. McSwain, C.E. Bates, Surface and interfacial energy relationships controlling graphite formation in cast iron, in *The Metallurgy of Cast Iron*, ed. by B. Lux, I. Minkoff, F. Mollard (Georgi Publishing, St. Saphorin, 1975), pp. 423–442
88. S.V. Subramanian, D.A.R. Kay, G.R. Purdy, Graphite morphology control in cast iron, in *The Physical Metallurgy of Cast Iron*, ed. by H. Fredriksson, M. Hillert, Stockholm, Mat. Res. Soc. Symposia Proc., North-Holland, NY, 1985, pp.47–56
89. G.H. Gilmer, in *Modeling of Casting and Welding Processes*, ed. by H.D. Brody, D. Apelian, (Metallurgical Soc. of AIME, 1981), pp. 385–401, ISBN-10: 0895203804
90. W.C. Johnson, H.B. Smartt, The role of interphase boundary adsorption in the formation of spheroidal graphite in cast iron. *Metall. Trans. A* **8A**, 553–565 (1977)
91. W.C. Johnson, H.B. Smartt, in *Solidification and Casting of Metals* (The Metal Society, 1979), Book No. 192 p. 129
92. J.S. Park, J.D. Verhoeven, Transitions between Type A flake, Type D flake, and coral graphite eutectic structures in cast irons. *Metall. Mater. Trans. A* **27A**, 2740–2753 (1996)
93. H.M. Muhmond, H. Fredriksson, Relationship between the trace elements and graphite growth morphologies in cast iron. *Metall. Mater. Trans.* **45A**, 6187–6199 (2014)